Atmospheric
Chemistry
and Physics

The semiannual oscillation (SAO) in the tropical middle atmosphere and its gravity wave driving in reanalyses and satellite observations

Manfred Ern[1], **Mohamadou Diallo**[1], **Peter Preusse**[1], **Martin G. Mlynczak**[2], **Michael J. Schwartz**[3], **Qian Wu**[4], **and Martin Riese**[1]

[1]Institut für Energie- und Klimaforschung – Stratosphäre (IEK-7), Forschungszentrum Jülich GmbH, 52425 Jülich, Germany
[2]NASA Langley Research Center, Hampton, Virginia, USA
[3]Jet Propulsion Laboratory, California Institute of Technology, Pasadena, California, USA
[4]National Center for Atmospheric Research, High Altitude Observatory, Boulder, Colorado, USA

Correspondence: Manfred Ern (m.ern@fz-juelich.de)

Abstract. Gravity waves play a significant role in driving the semiannual oscillation (SAO) of the zonal wind in the tropics. However, detailed knowledge of this forcing is missing, and direct estimates from global observations of gravity waves are sparse. For the period 2002–2018, we investigate the SAO in four different reanalyses: ERA-Interim, JRA-55, ERA-5, and MERRA-2. Comparison with the SPARC zonal wind climatology and quasi-geostrophic winds derived from Microwave Limb Sounder (MLS) and Sounding of the Atmosphere using Broadband Emission Radiometry (SABER) satellite observations show that the reanalyses reproduce some basic features of the SAO. However, there are also large differences, depending on the model setup. Particularly, MERRA-2 seems to benefit from dedicated tuning of the gravity wave drag parameterization and assimilation of MLS observations. To study the interaction of gravity waves with the background wind, absolute values of gravity wave momentum fluxes and a proxy for absolute gravity wave drag derived from SABER satellite observations are compared with different wind data sets: the SPARC wind climatology; data sets combining ERA-Interim at low altitudes and MLS or SABER quasi-geostrophic winds at high altitudes; and data sets that combine ERA-Interim, SABER quasi-geostrophic winds, and direct wind observations by the TIMED Doppler Interferometer (TIDI). In the lower and middle mesosphere the SABER absolute gravity wave drag proxy correlates well with positive vertical gradients of the background wind, indicating that gravity waves contribute mainly to the driving of the SAO eastward wind

phases and their downward propagation with time. At altitudes 75–85 km, the SABER absolute gravity wave drag proxy correlates better with absolute values of the background wind, suggesting a more direct forcing of the SAO winds by gravity wave amplitude saturation. Above about 80 km SABER gravity wave drag is mainly governed by tides rather than by the SAO. The reanalyses reproduce some basic features of the SAO gravity wave driving: all reanalyses show stronger gravity wave driving of the SAO eastward phase in the stratopause region. For the higher-top models ERA-5 and MERRA-2, this is also the case in the lower mesosphere. However, all reanalyses are limited by model-inherent damping in the upper model levels, leading to unrealistic features near the model top. Our analysis of the SABER and reanalysis gravity wave drag suggests that the magnitude of SAO gravity wave forcing is often too weak in the free-running general circulation models; therefore, a more realistic representation is needed.

1 Introduction

In the tropics, the zonal wind in the middle atmosphere exhibits characteristic oscillations of semiannual and quasi-biennial periods. The quasi-biennial oscillation (QBO) has an average period of 28 months and is the dominant mode in the stratosphere. The semiannual oscillation (SAO) dominates in the upper stratosphere and in the mesosphere with one amplitude peak in the stratopause region, the stratopause

semiannual oscillation (SSAO), and another amplitude peak somewhat below the mesopause, the mesopause semiannual oscillation (MSAO). For further details regarding the QBO and the SAO, please see Baldwin et al. (2001).

First observations of the SAO winds were made by rocket-sondes and radars at single stations in the tropics (e.g., Reed, 1966; Groves, 1972; Hirota, 1978; Dunkerton, 1982; Hamilton, 1982; Palo and Avery, 1993), and observations at tropical stations are still continued (e.g., Gurubaran and Rajaram, 2001; Venkateswara Rao et al., 2012; Day and Mitchell, 2013; Kishore Kumar et al., 2014). Direct observations of the SAO winds from satellite were made, for example, by the High Resolution Doppler Imager (HRDI) aboard the Upper Atmosphere Research Satellite (UARS) (e.g., Lieberman et al., 1993; Burrage et al., 1996) or by the Superconducting Submillimeter-Wave Limb-Emission Sounder (SMILES) instrument aboard the International Space Station (e.g., Baron et al., 2013).

Based on multiple observations including HRDI zonal winds, a first comprehensive climatology of the SAO in the tropical middle atmosphere was introduced by Garcia et al. (1997). A later assessment led to the Stratosphere-troposphere Processes And their Role in Climate (SPARC) global monthly climatology of zonal mean winds (Swinbank and Ortland, 2003; Randel et al., 2002, 2004). Unfortunately, direct global wind observations from satellite in the stratosphere and mesosphere are sparse. Therefore, Smith et al. (2017) recently investigated whether it is possible to interpolate quasi-geostrophic winds derived from Sounding of the Atmosphere using Broadband Emission Radiometry (SABER) and Microwave Limb Sounder (MLS) satellite observations into the tropics. Useful results were obtained for altitudes below about 80 km.

The SAO plays an important role in the whole atmosphere system. Effects of the SAO are also observed in temperatures (e.g., Reed, 1962; Delisi and Dunkerton, 1988a; Garcia and Clancy, 1990; Huang et al., 2008), and the SAO modulates the distribution of trace species in the stratosphere (e.g., Shu et al., 2013), as well as in the mesosphere and lower thermosphere (MLT) (e.g., Huang et al., 2008; Kumar et al., 2011; Zhu et al., 2015). It was found that the QBO and the SAO interact with each other. For example, the phases of the QBO and SAO can synchronize (e.g., Dunkerton and Delisi, 1997; Krismer et al., 2013), and eastward phases of the SAO can initiate QBO eastward phases (e.g., Kuai et al., 2009). This effect of the SAO is of relevance, because the QBO couples to the extratropics (e.g., Holton and Tan, 1980; Anstey and Shepherd, 2014) and has effects on surface weather and climate (e.g., Ebdon, 1975; Marshall and Scaife, 2009; Kidston et al., 2015). Climate and weather models have difficulties to simulate this influence of the QBO (e.g., Scaife et al., 2014). Further, there is evidence that both the QBO and the SAO influence the timing of sudden stratospheric warmings (e.g., Pascoe et al., 2006), and a correct representation of the SAO is needed to explain and better predict such extreme polar

vortex events and their influence on surface weather conditions (Gray et al., 2020). For these reasons, it is very important to learn more about the mechanisms that drive the SAO.

It is known that atmospheric gravity waves contribute to the driving of both the QBO and the SAO. As was shown by several model studies, particularly gravity waves generated by deep convection in the tropics should contribute significantly to the driving of the QBO and the stratopause SAO (e.g., Beres et al., 2005; Kim et al., 2013; Kang et al., 2018), as well as to the mesopause SAO (e.g., Beres et al., 2005). While critical level filtering of gravity waves of either eastward- or westward-directed phase speed plays a major role for the driving of the QBO (e.g., Lindzen and Holton, 1968; Lindzen, 1987; Dunkerton, 1997; Baldwin et al., 2001; Ern et al., 2014), the situation is more complicated for the SAO. It was suggested that the forcing of the stratopause SAO should be asymmetric, because gravity waves are selectively filtered by the QBO in the stratosphere before entering the altitude range dominated by the SAO (e.g., Hamilton and Mahlmann, 1988; Dunkerton and Delisi, 1997). The QBO westward phase has a stronger magnitude; therefore, a larger part of the gravity wave spectrum at westward-directed phase speeds is filtered out by encountering critical levels. For the stratopause region, this means that the gravity wave spectrum is dominated by eastward-propagating waves. Due to this excess of eastward momentum, gravity waves should mainly contribute to the driving of the SAO eastward phase and only to a lesser extent to the driving of the SAO westward phase. Instead, the driving of the SAO westward phase should be dominated by horizontal advection and the influence of planetary waves from the extratropics (e.g., Delisi and Dunkerton, 1988b; Hamilton and Mahlmann, 1988).

For the stratopause SAO, this asymmetry was confirmed by High Resolution Dynamics Limb Sounder (HIRDLS) satellite observations of gravity waves (Ern et al., 2015). Semiannual modulations of the global distribution of gravity waves are indeed observed over a large altitude range in the tropical mesosphere (e.g., Kovalam et al., 2006; Krebsbach and Preusse, 2007; Sridharan and Sathishkumar, 2008; Venkateswara Rao et al., 2012; Matsumoto et al., 2016; Chen et al., 2019). However, there is large uncertainty in which way those gravity waves contribute to the driving of the SAO and how far the aforementioned asymmetry of gravity wave driving extends upward into the mesosphere. Recent work by Smith et al. (2020) revealed that current global climate models have difficulties in simulating a realistic SSAO. One of the main reasons that was identified is a general lack of eastward forcing by waves in the model – either by large-scale waves or by gravity waves. Therefore, validation of the SAO wave forcing would be required. Another recent study shows that also in current meteorological reanalyses the SSAO differs strongly between the different reanalyses (Kawatani et al., 2020).

The mesopause SAO is out of phase with or even in antiphase with the SAO at lower altitudes (e.g., Hirota, 1980;

Dunkerton, 1982; Hamilton, 1982). Of course, not only gravity waves but also advection and medium-scale and global-scale waves (including tides) contribute to the driving of the SAO in the MLT region (e.g., Sassi and Garcia, 1997; Richter and Garcia, 2006). However, a likely reason for this out-of-phase relationship is the selective wave filtering of gravity waves by the SSAO and the SAO in the middle mesosphere. After the selective filtering of the gravity wave spectrum by the background winds, the spectrum is dominated by gravity waves propagating opposite to the wind direction, either eastward or westward, in the middle and lower mesosphere. This is confirmed, for example, by radar observations of gravity wave momentum fluxes (e.g., Matsumoto et al., 2016). If these remaining waves saturate and break in the upper mesosphere and the mesopause region, this results in driving of either the eastward or westward SAO phase, opposite to the wind in the middle mesosphere (e.g., Dunkerton, 1982; Mengel et al., 1995). This mechanism is also supported by HRDI wind observations (Burrage et al., 1996), as well as by model simulations (see, for example, Richter and Garcia, 2006; Peña-Ortiz et al., 2010). To some extent, even selective wave filtering by the QBO in the stratosphere has effects on the mesopause SAO (e.g., Garcia and Sassi, 1999; Lieberman et al., 2006; Peña-Ortiz et al., 2010). Overall, the driving of the MSAO is not fully understood, and observations of gravity wave momentum flux at the Equator are needed to resolve this issue, as stated in a recent review by Vincent (2015).

Our study investigates the SAO and its gravity wave driving in the whole middle atmosphere in the altitude range 30–90 km. We focus on the latitude range 10° S–10° N and the years 2002–2018 for which satellite data are available. For four reanalyses – the ERA-Interim and ERA-5 reanalyses of the European Centre for Medium-Range Weather Forecasts (ECMWF), the Japanese 55-year Reanalysis (JRA-55) of the Japan Meteorological Agency (JMA), and the Modern-Era Retrospective Analysis for Research and Applications, Version 2 (MERRA-2) reanalysis of the National Aeronautics and Space Administration (NASA) – we determine the zonal winds averaged over 10° S–10° N, and we estimate the driving of the SAO by gravity waves from the residual term (*missing drag*) in the transformed Eulerian mean (TEM) zonal-average momentum budget (e.g., Andrews et al., 1987; Alexander and Rosenlof, 1996). We also investigate the SAO in quasi-geostrophic zonal winds derived from satellite observations of the MLS and the SABER satellite instruments and in the winds directly observed by the TIMED Doppler Interferometer (TIDI) satellite instrument. Both SABER and TIDI are on the Thermosphere, Ionosphere, Mesosphere Energetics and Dynamics (TIMED) satellite. Further, we investigate the gravity wave driving of the SAO based on absolute gravity wave momentum fluxes and a proxy for absolute values of gravity wave drag derived from SABER satellite observations, and a correlation analysis between zonal winds and absolute gravity wave drag is carried out to reveal details of the SAO gravity wave driving.

The article is organized as follows. Section. 2 gives a description of the four reanalyses used in our study, and Sect. 3 gives a description of the instruments that provided the satellite data used in our study. In Sect. 4 we discuss the SAO zonal winds in the reanalyses (Sect. 4.1) and the SAO zonal winds derived from satellite data (Sect. 4.2). The winds derived from satellite data are quasi-geostrophic winds determined from SABER and MLS observations, as well as direct wind observations by TIDI. The SAO gravity wave driving expected from the reanalysis zonal momentum budget is discussed in Sect. 5, and in Sect. 6 we discuss the driving of the SAO based on SABER observations of absolute gravity wave momentum fluxes and the SABER absolute gravity wave drag proxy. A correlation analysis is carried out in Sect. 7 to investigate the relation between the SABER absolute gravity wave drag proxy and the SAO in more detail, and in Sect. 8 a similar correlation analysis is carried out for the reanalyses. Finally, Sect. 9 gives a summary of the paper.

2 Reanalysis data

In this paper four different meteorological reanalyses are used, interpolated to a longitude and latitude resolution of $1° \times 1°$. For a summary of different reanalyses, see also, for example, Fujiwara et al. (2017) and Martineau et al. (2018). The reanalysis ERA-Interim (see also Dee et al., 2011) of the European Centre for Medium-Range Weather Forecasts (ECMWF) has a horizontal model resolution of T255, corresponding to a longitudinal grid spacing of ~ 79 km at the Equator. It uses 60 levels in the vertical with a model top level at 0.1 hPa, i.e., somewhat above the stratopause (see also Fig. 1). A parameterization of orographic gravity waves after Lott and Miller (1997) is included. A parameterization for nonorographic gravity waves, however, is missing and only included in later ECMWF model versions (see also Orr et al., 2010). To avoid reflection of model-resolved waves at the model top, artificial damping (Rayleigh friction) is used at pressures lower than 10 hPa (altitudes above ~ 32 km).

The Japanese 55-year Reanalysis (JRA-55) (see also Kobayashi et al., 2015) of the Japan Meteorological Agency (JMA) has a finer grid spacing with a horizontal resolution of T319 (~ 55 km at the Equator). Like ERA-Interim, JRA-55 uses 60 model levels with the model top level at 0.1 hPa (see Fig. 1); a parameterization of orographic gravity waves is included (Iwasaki et al., 1989a, b), but there is no parameterization for nonorographic gravity waves. Rayleigh damping is applied at pressures below 50 hPa (altitudes above ~ 21 km). In addition, the horizontal diffusion coefficient is gradually increased with altitude at pressures lower than 100 hPa.

Unlike ERA-Interim and JRA-55, the Modern-Era Retrospective Analysis for Research and Applications, Version 2 (MERRA-2) reanalysis (see also Gelaro et al., 2017) uses 72 layers in the vertical with a model top at 0.01 hPa and a top
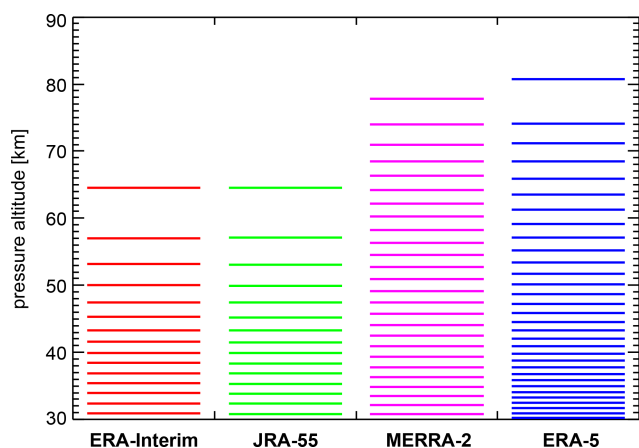
Figure 1. Altitude levels of the four reanalyses in the approximate altitude range 30 to 90 km used in this study. Altitudes given in this figure are pressure altitudes using a fixed pressure scale height of 7 km.

layer mid level at 0.015 hPa ($\sim$ 78 km) in the upper mesosphere. The horizontal resolution is 0.5° latitude $\times$ 0.625° longitude. Parameterizations for both orographic (McFarlane, 1987) and nonorographic gravity waves (Garcia and Boville, 1994; Molod et al., 2015) are included. Additional damping is applied at pressures less than 0.24 hPa (altitudes above $\sim$ 58 km), i.e., at altitudes much higher than in ERA-Interim and JRA-55. One peculiarity of MERRA-2 is that, starting in August 2004, MLS temperature data are assimilated. This means that MERRA-2 is constrained by observations even in the mesosphere, while other reanalyses usually do not include observations above the stratosphere. Further, the MERRA-2 nonorographic gravity wave drag scheme was optimized for a better representation of the QBO and the SAO in the tropics (Molod et al., 2015).

Similar to MERRA-2, the ECMWF reanalysis ERA-5 (see also Hersbach and Dee, 2016; Hersbach et al., 2018, 2019, 2020) has a high model top with the top level at 0.01 hPa ($\sim$ 80 km). The number of model levels is 137, resulting in a better vertical resolution than for all reanalyses previously described, including MERRA-2 (Fig. 1). The horizontal resolution is T639, according to a longitudinal grid spacing of $\sim$ 31 km at the Equator. In our work we use the updated version ERA5.1 that uses an improved assimilation scheme for the period 2000–2006 (Simmons et al., 2020). ERA-5 uses parameterizations for orographic (Lott and Miller, 1997; Sandu et al., 2013) and nonorographic (Orr et al., 2010) gravity waves but does not assimilate MLS data. The sponge layer starts at pressures lower than 10 hPa (altitudes above $\sim$ 32 km) and depends on model level and zonal wavenumber in order to damp vertically propagating waves (e.g., Polichtchouk et al., 2017). An additional sponge layer starts at pressures lower than 1 hPa (altitudes above $\sim$ 48 km). Unlike ERA-Interim, no Rayleigh friction is applied at pressures lower than 10 hPa. For comparison, Fig. 1

illustrates the model levels used in the different reanalyses for the altitude range of 30 to 90 km covered in this study.

3 The satellite instruments MLS, SABER, and TIDI

The Microwave Limb Sounder (MLS) is one of the instruments aboard the NASA satellite Aura. MLS is a limb sounding radiometer that observes atmospheric microwave emissions (e.g., Waters et al., 2006; Livesey et al., 2017). From these limb observations, atmospheric temperature and a number of trace species are derived. In our study we use MLS version 4.2 atmospheric temperatures and geopotential height, which are available from the middle troposphere to the mesopause region (pressures from 316 to 0.001 hPa). The vertical resolution is between $\sim$ 4 km in the stratosphere and $\sim$ 14 km around the mesopause. A detailed description of the temperature/pressure retrieval is given, for example, in Schwartz et al. (2008). The Aura satellite is in a Sun-synchronous orbit. Therefore, MLS observations are always at two fixed local solar times. In the tropics, these local times are about 13:45 LST (local solar time) for the ascending orbit parts (i.e., when the satellite is flying northward) and 01:45 LST for the descending orbit parts (i.e., when the satellite is flying southward), according to the satellite Equator crossing times. Measurements of MLS started on 8 August 2004 and are still ongoing at the time of writing.

The Sounding of the Atmosphere using Broadband Emission Radiometry (SABER) instrument was launched with the Thermosphere, Ionosphere, Mesosphere Energetics and Dynamics (TIMED) satellite in December 2001. SABER measurements started on 25 January 2002 and are still ongoing at the time of writing. TIMED has been approved to operate for 3 more years, until September 2023. Another 3 more years of operations will be proposed in the near future. SABER is a broadband radiometer that observes atmospheric infrared emissions in limb-viewing geometry with an altitude resolution of about 2 km. Atmospheric temperatures are derived from infrared emissions of carbon dioxide (CO_2) at around 15 µm. The SABER temperature/pressure retrieval is described in detail by Remsberg et al. (2004) and Remsberg et al. (2008). More details on the SABER instrument are given, for example, in Mlynczak (1997) and Russell et al. (1999). In our study we use SABER version 2 temperatures, and in Sect. 6.1 we briefly introduce the method how absolute gravity wave momentum fluxes and a proxy for absolute gravity wave drag can be derived from these temperature observations.

The TIMED satellite orbit is slowly precessing with a period of about 120 d. To ensure that always the same side of the satellite stays in the dark, TIMED performs yaw maneuvers approximately every 60 d. Accordingly, the local solar time of the satellite observations slowly drifts over one of the $\sim$ 60 d periods and then jumps when a satellite yaw is performed. This is illustrated for the equatorial local solar times

of SABER observations for the time period 2002 until 2018 in Fig. S1 in the Supplement of this paper.

Since launch, the TIMED spacecraft has been decreasing in altitude by about $1 \, \mathrm{km \, yr^{-1}}$. The inclination of the spacecraft has remained stable at 74°. However, the change in altitude has resulted in a drift of local time sampling and hence of the yaw date. The first TIMED yaw was in January 2002. At the time of writing, that yaw is now occurring in late December. As a consequence, the local time sampled in a given day or month changes every year. This effect could affect trend studies but should not impact our work.

Another instrument aboard the TIMED satellite is the TIMED Doppler Interferometer (TIDI). Detailed information about TIDI can be found, for example, in Killeen et al. (2006) or Niciejewski et al. (2006). The TIDI instrument is a Fabry–Pérot interferometer that was designed to observe atmospheric winds in the altitude range 70–120 km with an altitude resolution of about 2 km. This is achieved by using four separate telescopes to observe atmospheric emissions of rotational lines in the molecular oxygen (O_2) (0–0) band around 762 nm in limb-viewing geometry. One pair of telescopes is located on the sunlit side of the TIMED satellite (warm side), and the other pair is located on the dark side (cold side). In each pair, one telescope views forward at an angle of 45° with respect to the satellite velocity vector, and the other telescope views 45° backward. In this way, the same air volume is observed by the two telescopes of a pair with a time difference of only 9 min. Based on these orthogonal measurements, wind vectors can be derived from the Doppler shift of the atmospheric emissions. The wind vector observations form two tracks on either side of the spacecraft, i.e., the warm side and the cold side. These two tracks are at different local solar times with the local solar time of the cold side track differing from the local solar time of the corresponding SABER observations by only about half an hour. (See also Fig. S1.) Like for SABER, also TIDI observations are still ongoing at the time of writing.

4 The SAO zonal wind in reanalyses and satellite data

4.1 The SAO in the reanalyses ERA-Interim, JRA-55, ERA-5, and MERRA-2

In our study, we focus on the 2002–2018 period, because gravity wave observations by the SABER instrument are available only starting from 2002. From the reanalyses, we use global distributions of meteorological fields at 00:00, 06:00, 12:00, and 18:00 UT. For comparison with SABER data, we calculate values of the zonal wind averaged over 7 d and over the latitude band 10° S–10° N. Values are calculated in steps of 3 d, i.e., the time periods used for averaging are overlapping.

For the four reanalyses considered, Fig. 2a–d show the variations of the zonal wind in the tropics for the *typical*

year. This *typical year* is obtained by averaging the zonal wind over the latitude band 10° S–10° N and the years from 2002 until 2018. Distributions for the single years are shown in the Supplement of this paper.

For guiding the discussion, Fig. 2e shows also the zonal wind of the SPARC zonal wind climatology, averaged over the latitude band 10° S–10° N. The SPARC wind climatology is a monthly climatology that is based on the UARS (Upper Atmosphere Research Satellite) Reference Atmosphere Project (URAP) wind climatology (Swinbank and Ortland, 2003; Randel et al., 2002, 2004). For the time period 1992–1998, it combines wind observations by the High Resolution Doppler Imager (HRDI) instrument on UARS (see Hays et al., 1993) and model data to interpolate gaps. There are several uncertainties that potentially affect this climatology:

 – There may be wind biases due to uncertainties of the zero-wind – an inherent problem of wind observations based on the Doppler shift method applied from a satellite (e.g., Hays et al., 1993; Baron et al., 2013).

 – HRDI observations are during daytime only. Although a correction of tidal effects was applied, there could be remaining biases.

 – In the period 1992–1998 there are only about 4.5 years of quasi-continuous HRDI observations. Therefore, interannual variability will still have a strong effect on the monthly averages of the SPARC climatology.

 – HRDI data gaps had to be interpolated for the climatology. This could introduce biases and interpolation artifacts. In particular, there is a HRDI data gap centered around 0.3 hPa (~ 55 km altitude). In Sect. 4.1.2 we will discuss whether the continuously eastward-directed winds at this altitude could be a reliable feature.

In spite of these shortcomings, at SAO altitudes the SPARC climatology is still the only global climatology based on direct wind observations, and it summarizes our poor knowledge of the SAO. Therefore, this climatology is very useful for guiding the discussion throughout the paper. However, given the above uncertainties, the SPARC climatology should not be considered a reference or the "truth".

4.1.1 The stratopause SAO

All reanalyses capture some basic features of the SAO in the stratopause region and in the lower mesosphere. In all reanalyses, the first SAO period of a given year has the larger amplitude, as expected from observations (e.g., Garcia et al., 1997; Swinbank and Ortland, 2003). It is noteworthy that, while there is strong interannual variability in all reanalyses, this variability differs strongly among the different reanalyses; see Figs. S2–S5. There are also other significant differences. For example, in ERA-Interim, the eastward winds of the first SAO period of a given year are somewhat stronger
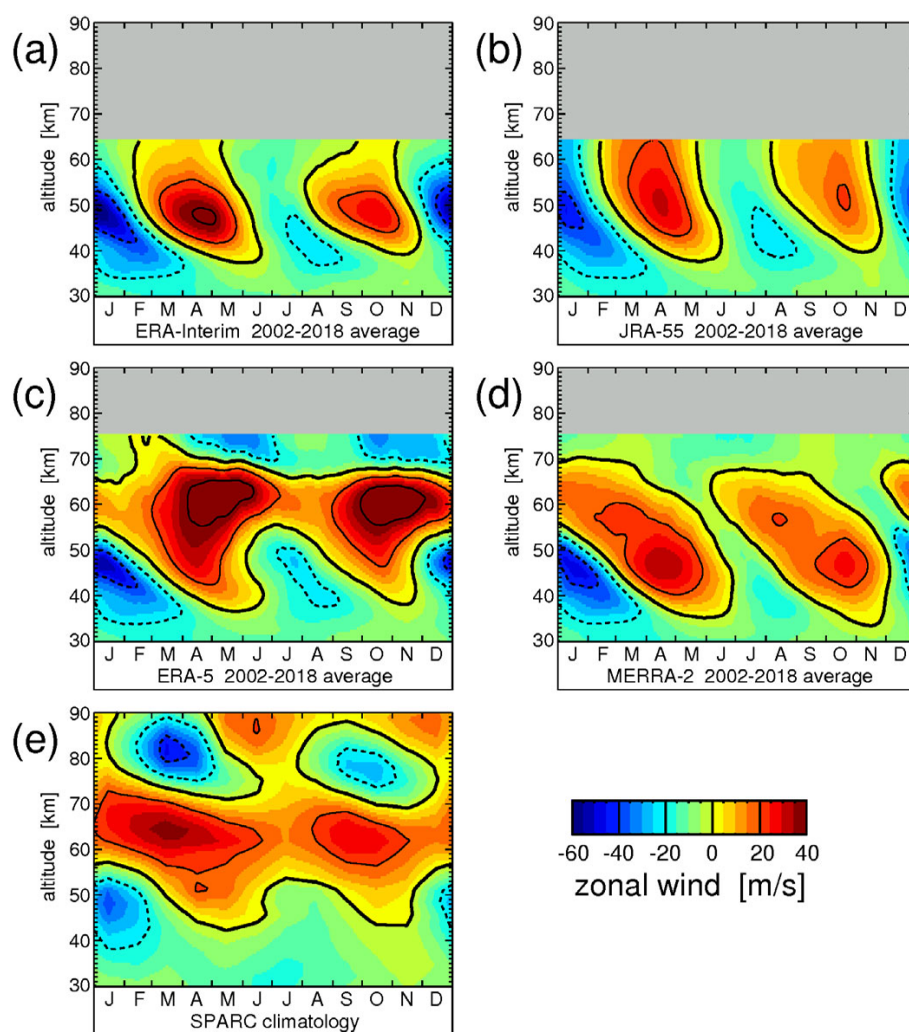
Figure 2. Typical seasonal variation of the zonal-average zonal wind averaged over 10° S–10° N and the time period 2002–2018 for the four reanalyses **(a)** ERA-Interim, **(b)** JRA-55, **(c)** ERA-5, and **(d)** MERRA-2. For comparison, **(e)** shows the corresponding zonal winds of the SPARC climatology (see Swinbank and Ortland, 2003; Randel et al., 2002, 2004). Overlaid are contour lines of the respective wind data set. Contour line increment is $20\,\mathrm{m\,s^{-1}}$. The zero wind line is highlighted in bold solid contour lines, and westward (eastward) winds are indicated by dashed (solid) contour lines.

than in JRA-55, or in MERRA-2. Further, ERA-5 eastward jets are generally too strong at altitudes above $\sim 45\,\mathrm{km}$, consistent with previous studies (Hersbach et al., 2018; Shepherd et al., 2018). These overly strong eastward winds are caused by severe tapering of vorticity errors in the mesosphere, and this issue has been resolved from the introduction of IFS cycle 43r3 (11 July 2017) (Hersbach et al., 2018).

Generally, large differences at high altitudes result, because ERA-Interim and JRA-55 have lower model tops and introduce stronger artificial damping at lower altitudes than in MERRA-2 and ERA-5. Therefore, ERA-Interim winds strongly weaken at altitudes above 50 km, which, however, is less the case for JRA-55.

Compared to the SPARC climatology, the SAO in all four reanalyses has a larger amplitude in the upper stratosphere.

Partly, this is caused by the fact that the SPARC climatology has only a monthly temporal resolution and will therefore smear out rapid temporal changes like the SAO. In addition, some of the abovementioned error sources could affect the SPARC climatology.

4.1.2 The SAO in the mesosphere and the MSAO

At altitudes above $\sim 60\,\mathrm{km}$, deviations between the SPARC climatology and the reanalyses become large. In the SPARC climatology at altitudes between 60 and 70 km, the zonal wind is continuously eastward, which, on average, is only the case in ERA-5. In ERA-5, however, eastward-directed winds in this altitude range are often too strong.

These eastward-directed winds around 60 and 70 km altitude seem to be a real feature in climatological averages. For example, continuously eastward winds at the Equator have been observed around 0.1 hPa ($\sim$ 65 km) from October 2009 until April 2010 by the Superconducting Submillimeter-Wave Limb-Emission Sounder (SMILES) instrument (Baron et al., 2013). During this period also in MERRA-2 eastward winds are seen around $\sim$ 65 km but not in a multi-year average. Also multi-year averages of quasi-geostrophic winds that are derived from satellite observations and interpolated to the tropics show persistent eastward winds around $\sim$ 65 km. There is, however, strong interannual variability, and in several years it is observed that the zonal winds at altitudes around $\sim$ 65 km alternate between eastward and westward due to the SAO (see Smith et al., 2017, and Sects. 4.2.2 and 4.2.3).

Another important feature in the SPARC climatology is a mesopause SAO that is in an anti-phase relation with the SAO at lower altitudes (see also, for example, Burrage et al., 1996) and has its peak amplitude around $\sim$ 80 km. Of course, the MSAO is not captured by ERA-Interim and JRA-55 because of their low model tops. Also MERRA-2 does not capture the MSAO. Due to a strong sponge layer, the zonal wind in MERRA-2 is gradually damped to near zero close to the model top. Only ERA-5 partly captures the MSAO, and the wind reverses to westward at altitudes around 70 km, i.e., near the model top.

4.2 The SAO as seen in satellite data

4.2.1 Interpolated quasi-geostrophic winds in the tropics

Following the approach used in previous studies (e.g., Oberheide et al., 2002; Ern et al., 2013; Smith et al., 2017; Sato et al., 2018), quasi-geostrophic winds can be calculated from the geopotential fields derived from satellite soundings. For stationary conditions and neglecting the drag exerted by atmospheric waves, the zonal and meridional momentum equations can be written as follows

$$-\left(f + \frac{u\tan\phi}{a}\right)v + \frac{1}{a\cos\phi}\frac{\partial\Phi}{\partial\lambda} = 0, \tag{1}$$

$$\left(f + \frac{u\tan\phi}{a}\right)u + \frac{1}{a}\frac{\partial\Phi}{\partial\phi} = 0. \tag{2}$$

Here, u and v are the zonal and the meridional wind, respectively; a the Earth's radius; ϕ the geographic latitude; and Φ the geopotential. For further details, see Andrews et al. (1987), Oberheide et al. (2002), or Ern et al. (2013). These equations can be easily solved for u and v.

The quasi-geostrophic approach gives good results in the extratropics, but it is not reliable in the tropics, because the Coriolis parameter is close to zero. Recently, it has been shown by Smith et al. (2017) that an interpolation of the quasi-geostrophic zonal wind starting from 10° S and 10° N

can be used as a proxy for the zonal wind at the Equator, and it is in good agreement with wind observations by lidar below about 80 km.

As direct wind observations in the tropical mesosphere are sparse, we will also make use of this approach, even though interpolated quasi-geostrophic winds will still be affected by biases. In order to make sure that our findings are robust, we will use a number of different zonal wind data sets in Sects. 6 and 7 to check whether our findings of the SAO gravity wave driving hold for different choices of background winds.

For our study, we utilize zonal-average quasi-geostrophic zonal winds calculated for time intervals of 3 d with a time step of 3 d, i.e., the time windows used for calculating the winds are non-overlapping. This data set has been previously used for studies in the extratropics (Ern et al., 2013, 2016; Matthias and Ern, 2018). For studying the interaction of gravity waves with the SAO zonal wind in the latitude band 10° S–10° N, we use the average of the quasi-geostrophic wind at 12° S and 12° N as a proxy for the zonal wind in this latitude band at altitudes above 45 km, similarly as in Smith et al. (2017). At lower altitudes, reanalysis winds should be more reliable, so we do not use quasi-geostrophic winds at altitudes below 35 km. Instead, we use the ERA-Interim winds presented in Fig. 2a (and in Fig. S2), and a smooth transition between ERA-Interim and quasi-geostrophic winds derived from SABER or MLS satellite observations in the altitude range 35–45 km.

4.2.2 MLS quasi-geostrophic winds

For comparison with the MERRA-2 reanalysis that assimilates MLS data, Fig. 3a shows the average year of the merged data set of ERA-Interim and interpolated MLS quasi-geostrophic winds. As MLS observations started in mid-2004, averaging was performed only over the years 2004 until 2018. To reduce the effect of tides, MLS winds are calculated from an average over ascending and descending orbit branches; i.e., data from the two MLS Equator crossing times are averaged.

Figures 2d and 3a show that at altitudes below $\sim$ 60 km MLS and MERRA-2 winds are very similar. For the single years, this is also seen from Figs. S5 and S6. On the one hand, this is expected, because MLS data are assimilated in MERRA-2. On the other hand, this shows that our interpolated quasi-geostrophic winds are useful in the tropics. Still, these interpolated winds are not considered to be reliable at altitudes above $\sim$ 75 km. For example, above $\sim$ 75 km eastward winds are relatively strong, and the duration of the SAO westward wind phases at altitudes above $\sim$ 70 km is relatively short when compared with the other data sets. Both these effects could be an effect of tides. Although both ascending and descending nodes enter the estimation of MLS quasi-geostrophic winds, it is not expected that tidal effects will completely cancel out.
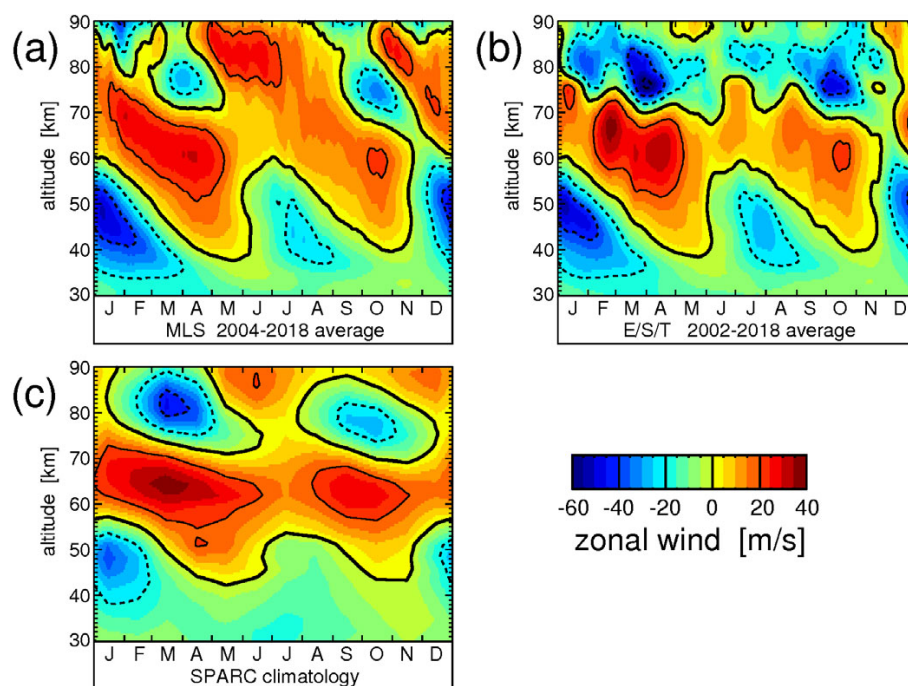
Figure 3. Typical seasonal variation of the zonal-average zonal wind averaged over 10° S–10° N and the time period 2002–2018 for two data sets that use satellite data. Panel **(a)** is a data set that uses ERA-Interim winds at altitudes < 35 km, MLS quasi-geostrophic winds at altitudes > 45 km, and a smooth transition between ERA-Interim and MLS winds between 35 and 45 km. Panel **(b)** is a data set called "E/S/T-winds" that uses ERA-Interim winds at altitudes < 35 km, SABER quasi-geostrophic winds at altitudes 45–75 km, and TIDI cold side winds, i.e., direct wind observations, at altitudes above 80 km. Between 35 and 45 km, there is a smooth transition between ERA-Interim and SABER winds. The gap between 75 and 80 km is interpolated. In **(a)** and **(b)**, MLS, SABER and TIDI winds are an average over ascending and descending orbit branches. For comparison, **(c)** shows the corresponding zonal winds of the SPARC climatology (see Swinbank and Ortland, 2003; Randel et al., 2002, 2004). Overlaid are contour lines of the respective wind data set. Contour line increment is 20 m s^{-1}. The zero wind line is highlighted in bold solid contour lines, and westward (eastward) winds are indicated by dashed (solid) contour lines.

4.2.3 Merged SABER quasi-geostrophic and TIDI wind observations

So far we have discussed wind data sets of four reanalyses, as well as interpolated quasi-geostrophic winds based on MLS observations. Another main purpose of our work is to study the interaction of SABER gravity wave observations with the background wind. Of course, both the SAO and tides contribute to the variations of the winds in the tropics. As shown in Fig. S1, the local solar times of SABER Equator crossings slowly change over time. Therefore, it is important to compare gravity wave observations and winds observed at the same local solar times.

For this purpose, we have composed a combined data set of SABER quasi-geostrophic winds in the altitude range 45–75 km, ERA-Interim winds below 35 km, and a smooth transition between ERA-Interim and SABER winds in the altitude range 35–45 km. At altitudes above ∼ 80 km we use directly observed TIDI "cold side" winds. As shown in Fig. S1, the local solar time of TIDI cold side winds matches the local solar times of SABER observations better than about half an hour. Winds in the gap between 75 and 80 km are inter-

polated. Similarly as in the study of Dhadly et al. (2018), we omit less reliable TIDI data from periods when the angle β between orbital plane and the Earth–Sun vector exceeds 55°, i.e., when the TIMED orbital plane is near the terminator. Data gaps that are caused by omitting these data, as well as other data gaps that are shorter than 40 d are closed by linear interpolation in time. A larger data gap from November 2016 until March 2017 is closed by using interpolated SABER quasi-geostrophic winds also at altitudes above 75 km. Interpolated SABER quasi-geostrophic winds are used above 75 km also before April 2002, because TIDI cold side winds are available only after that date.

Figure 3b shows the 2002–2018 average year of this combined wind data set. Single years are shown in Fig. S7. In the following, this combined wind data set will be termed for convenience "E/S/T-winds". SABER and TIDI winds were averaged over ascending and descending TIMED satellite Equator passings; i.e., they represent an average over different local solar times. At altitudes below ∼ 70 km these winds are very similar to those derived from MLS (see Fig. 3a). Although ascending and descending orbit data are combined, there are notable variations that are related to the 60 d yaw

cycle of the TIMED satellite and the corresponding changes in the local solar time of SABER and TIDI observations. This shows the importance of selecting wind data at the correct local solar time, particularly at higher altitudes.

The main difference between Fig. 3a and b, however, are the winds at altitudes above 80 km where TIDI wind observations are used. On average, the TIDI winds are more westward than the quasi-geostrophic winds derived from MLS, and even somewhat more westward than the SPARC climatology (Fig. 3c). Particularly the maxima of both SAO eastward phases at altitudes above around 85 km are less pronounced. Because at altitudes above 80 km variations that are linked to the TIMED yaw cycles and the corresponding changes in local solar time are quite strong, this could be an effect of tides. The TIDI instrument samples atmospheric tides at the same phase as SABER. Since wind variations due to tides can be of the same magnitude as variations due to the SAO, the combined data set of SABER and TIDI winds should therefore be the best choice for representing the atmospheric background conditions relevant for SABER gravity wave observations.

A more comprehensive analysis of tides based on TIDI winds has been carried out in previous studies (e.g., Oberheide et al., 2006; Wu et al., 2011; Dhadly et al., 2018). An in-depth investigation of the effect of tides on the distribution of gravity waves, however, is beyond the scope of our study. Overall, the differences between the different wind data sets show the importance of further global wind observations in the upper mesosphere and lower thermosphere, and particularly in the tropics. As there are notable differences between different wind data sets, in Sect. 7 we will compare SABER gravity wave observations to several different wind data sets in order to find out which findings are robust and widely independent of the wind data used.

5 Gravity wave driving of the SAO in reanalyses

Given the limitations of the different reanalyses and the differences in the representation of the SAO, it is not expected that estimates of the SAO gravity wave driving from the reanalyses will be fully realistic. In particular the magnitude of the gravity wave driving might not be very robust. However, our knowledge of the driving of the SAO is relatively poor, and in Sect. 4.1 we have seen that all reanalyses are capable of reproducing some features of the SAO. Therefore, it is expected that estimates of the SAO gravity wave driving in reanalyses will provide important information about the mechanisms that drive the SAO. This information can already be obtained from relative variations of the gravity wave driving, and the exact magnitude is not needed.

5.1 Estimates of gravity wave drag from reanalyses

Based on the transformed Eulerian mean (TEM) zonal mean momentum budget, an expected value of the zonal-mean zonal gravity wave drag can be estimated from reanalyses. The zonal mean momentum equation is given by

$$\frac{\partial \overline{u}}{\partial t} + \overline{v}^* \left(\frac{(\overline{u} \cos \phi)_\phi}{a \cos \phi} - f \right) + \overline{w}^* \overline{u}_z = \overline{X}_{\mathrm{PW}} + \overline{X}_{\mathrm{GW}}. \qquad (3)$$

Here, $\overline{u}$ is the zonal-mean zonal wind, $\partial \overline{u}/\partial t$ is the zonal wind tendency, $\overline{v}^*$ and $\overline{w}^*$ are the TEM meridional and vertical wind, respectively, f is the Coriolis frequency, a is the Earth's radius, and ϕ is the geographic latitude. $\overline{X}_{\mathrm{PW}}$ and $\overline{X}_{\mathrm{GW}}$ are the zonal-mean zonal wave drag due to global-scale waves and gravity waves, respectively. Subscripts ϕ and z stand for differentiation in meridional and vertical direction, respectively. Overbars indicate zonal averages.

All terms in Eq. (3) except for $\overline{X}_{\mathrm{GW}}$ can be calculated from the resolved meteorological fields of the reanalysis. The resolution (both horizontally and vertically) of the general circulation models used in the reanalyses, however, is too coarse to properly resolve all scales of gravity waves. This means that part of the gravity wave spectrum is not resolved by the models, and amplitudes of resolved gravity waves are usually underestimated (e.g., Schroeder et al., 2009; Preusse et al., 2014; Jewtoukoff et al., 2015). Therefore, free-running general circulation models and reanalyses utilize parameterizations to simulate the contribution of gravity waves to the momentum budget (e.g., Fritts and Alexander, 2003; Kim et al., 2003; Alexander et al., 2010; Geller et al., 2013).

Unlike those of free-running models, the meteorological fields of reanalyses are constrained by assimilation of numerous observations. Where constrained by observations, the meteorological fields of reanalyses can be assumed to be quite realistic. Under this assumption, the contribution $\overline{X}_{\mathrm{GW}}$ in Eq. (3) can be calculated from the residual term (*missing drag*), remaining after quantifying all other contributions from the model-resolved fields (e.g., Alexander and Rosenlof, 1996; Ern et al., 2014, 2015).

Like in Ern et al. (2015), we calculate the zonal-mean zonal wave drag $\overline{X}_{\mathrm{res}}$ due to waves that are resolved by the model from the divergence of the Eliassen–Palm flux (EP flux). Further, we assume that the zonal drag due to global-scale waves can be approximated based on the resolved flux at zonal wavenumbers k lower than 21:

$$\overline{X}_{\mathrm{PW}} = \overline{X}_{\mathrm{res}}(k < 21). \qquad (4)$$

Under this assumption, our estimate of the *total* zonal mean gravity wave drag $\overline{X}_{\mathrm{GW}}$ comprises the drag of model-resolved waves at zonal wavenumbers higher than 20 ($\overline{X}_{\mathrm{res}}(k > 20)$), gravity wave drag that is parameterized in the model ($\overline{X}_{\mathrm{param}}$), and the remaining imbalance ($\overline{X}_{\mathrm{imbalance}}$) in the momentum budget that is caused by, for example, data assimilation:

$$\overline{X}_{\mathrm{GW}} = \overline{X}_{\mathrm{res}}(k > 20) + \overline{X}_{\mathrm{param}} + \overline{X}_{\mathrm{imbalance}}, \qquad (5)$$

with the *missing drag* consisting of the sum of $\overline{X}_{\mathrm{param}}$ and $\overline{X}_{\mathrm{imbalance}}$.

5.2 Discussion of the different contributions to $\overline{X}_{\mathrm{GW}}$

Figure 4 shows the *typical year* of the estimated *total* gravity wave drag $\overline{X}_{\mathrm{GW}}$ for the four reanalyses considered. Again, the *typical year* was obtained by averaging over the latitude band 10° S–10° N and the years 2002 until 2018. Distributions for the single years are shown in Figs. S8–S11.

5.2.1 Model-resolved gravity wave drag $\overline{X}_{\mathrm{res}}(k > 20)$

Similarly as Fig. 4, Fig. 5 shows the contribution $\overline{X}_{\mathrm{res}}(k > 20)$ of model-resolved gravity waves at zonal wavenumbers $k > 20$. The corresponding distributions for the single years are shown in Figs. S12–S15.

As can be seen from Figs. 4 and 5, the resolved gravity wave drag is negligible in ERA-Interim, JRA-55, and MERRA-2. (Please note that in Fig. 4 the range of the color scale is $\pm 7.5\,\mathrm{m\,s^{-1}\,d^{-1}}$, while it is only $\pm 0.25\,\mathrm{m\,s^{-1}\,d^{-1}}$ in Fig. 5a, b, and d, and $\pm 1.25\,\mathrm{m\,s^{-1}\,d^{-1}}$ in Fig. 5c.) Only for ERA-5 below 55 km $\overline{X}_{\mathrm{res}}(k > 20)$ sometimes contributes as much as about 50 % to $\overline{X}_{\mathrm{GW}}$. In the upper stratosphere and lower mesosphere, for both $\overline{X}_{\mathrm{GW}}$ and $\overline{X}_{\mathrm{res}}(k > 20)$ eastward gravity wave drag is stronger than westward gravity wave drag, which is likely a consequence of the QBO wave filtering in the stratosphere below.

Strictly speaking, introducing a zonal wavenumber limit of $k = 20$ in order to separate gravity waves from larger-scale atmospheric variations is somewhat arbitrary. In particular, it is assumed that gravity waves propagate mainly zonally. In the tropics, this assumption should be fulfilled since the gravity wave distribution is modulated by the background wind, and in the tropics zonal winds are usually much stronger than meridional winds. Further, the fact that for the reanalyses the resolved gravity wave drag $\overline{X}_{\mathrm{res}}(k > 20)$ contributes only to a minor extent to the total gravity wave drag $\overline{X}_{\mathrm{GW}}$ shows that the exact choice of a wavenumber threshold will not affect $\overline{X}_{\mathrm{GW}}$ by much. Therefore, it is not expected that different methods to extract gravity waves from the model fields – for example, by introducing thresholds using spherical coordinates (e.g., Watanabe et al., 2008; Becker and Vadas, 2018) – would lead to different conclusions.

5.2.2 Parameterized gravity wave drag $\overline{X}_{\mathrm{param}}$

For JRA-55 and MERRA-2 also the parameterized gravity wave drag is provided in the data repositories. Figure 6a shows the *typical year* of parameterized gravity wave drag $\overline{X}_{\mathrm{param}}$ for JRA-55, and Fig. 6b shows the same but for MERRA-2 (please note that for MERRA-2 $\overline{X}_{\mathrm{param}}$ is not available for the whole altitude range). Distributions for the single years 2002–2018 are shown in Figs. S16 and S17.

As can be seen from Fig. 6a, for JRA-55 the parameterized gravity wave drag $\overline{X}_{\mathrm{param}}$ is closely linked with and opposite

to the background wind. This is expected because JRA-55 does not have an explicit nonorographic gravity wave parameterization and uses only Rayleigh friction at upper levels. A similar distribution would be expected for ERA-Interim, because ERA-Interim also uses Rayleigh friction at upper levels and does not have a nonorographic gravity wave parameterization.

For MERRA-2 (Fig. 6b), the situation is completely different. Comparing Figs. 4d and 6b, it is evident that for MERRA-2 in the whole altitude range $\overline{X}_{\mathrm{GW}}$ and $\overline{X}_{\mathrm{param}}$ are almost the same, and both are linked more closely to the vertical gradient of the zonal wind and not to the zonal wind speed itself. Obviously, this is an effect of the MERRA-2 nonorographic gravity wave drag scheme (Garcia and Boville, 1994; Molod et al., 2015), which includes some realistic gravity wave physics instead of just using Rayleigh friction.

5.2.3 The imbalance gravity wave drag term $\overline{X}_{\mathrm{imbalance}}$

For JRA-55 and MERRA-2 also the imbalance term $\overline{X}_{\mathrm{imbalance}}$ can be calculated. For JRA-55 the *typical year* is given in Fig. 6c, and for MERRA-2 in Fig. 6d. The distribution for single years is given in Figs. S18 and S19.

As can be seen from Fig. 6c, for JRA-55, above 40 km the remaining imbalance is strongly positive. This likely indicates that a really large positive assimilation increment is needed to compensate the unrealistic effect of Rayleigh friction, and to keep the model temperature and winds in agreement with assimilated observations. The situation should be similar for ERA-Interim.

For MERRA-2, $\overline{X}_{\mathrm{imbalance}}$ (Fig. 6d) is close to zero. Apparently, in the tropics the nonorographic gravity wave drag scheme of MERRA-2 has been tuned in a way to minimize the assimilation increment caused by the assimilation of MLS and other data (see also Molod et al., 2015). This should be the reason why MERRA-2 simulates a reasonable SAO even in the years when MLS data were not yet available (i.e., in the period prior to August 2004).

5.3 Gravity wave driving of the SAO in ERA-Interim and JRA-55

Figure 4a and b show the *typical year* of the estimated *total* gravity wave drag $\overline{X}_{\mathrm{GW}}$ for ERA-Interim and JRA-55, respectively. In the altitude range 45–55 km total gravity wave drag $\overline{X}_{\mathrm{GW}}$ is usually directed eastward, contributing to the driving of the eastward phase of the stratopause SAO with a maximum value of about $5\,\mathrm{m\,s^{-1}\,d^{-1}}$. Westward gravity wave driving in the stratopause region is much weaker and, on average, does not contribute much to the driving of the stratopause SAO. This asymmetry has been pointed out before for ERA-Interim by Ern et al. (2015). At high altitudes, eastward gravity wave drag strongly increases, which is likely not realistic and an effect of the sponge layer close to
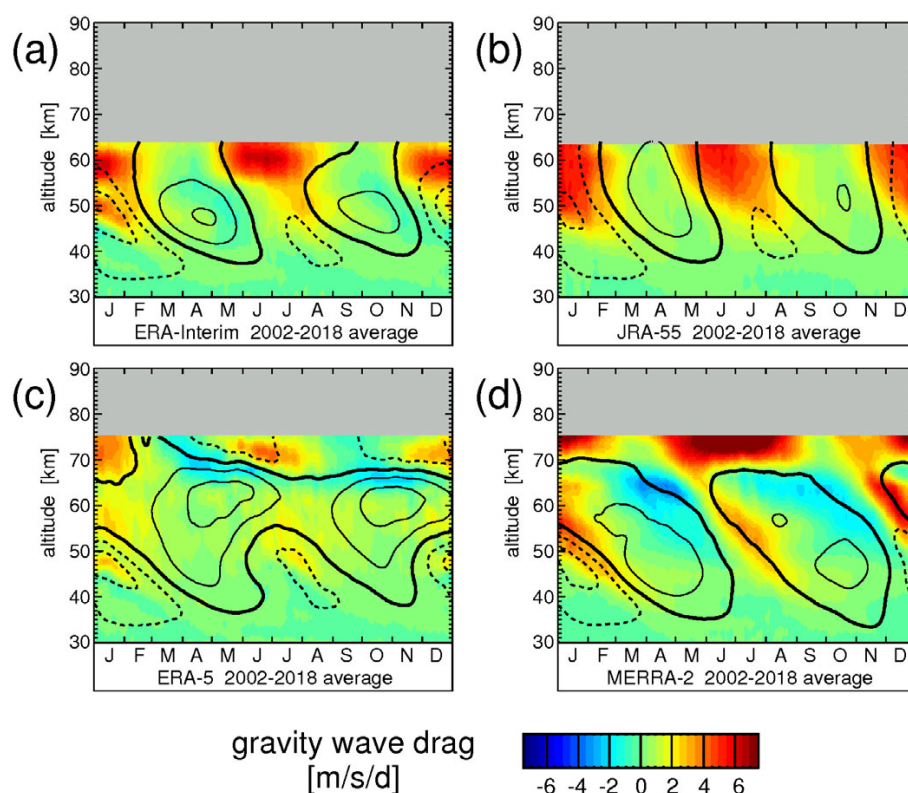
Figure 4. Typical seasonal variation of the *total* gravity wave drag $\overline{X}_{GW}$ estimated from the TEM momentum budget. The values are averages over $10°$ S–$10°$ N and the time period 2002–2018 for the four reanalyses **(a)** ERA-Interim, **(b)** JRA-55, **(c)** ERA-5, and **(d)** MERRA-2. Overlaid are contour lines of the respective wind data set. Contour line increment is $20\,\mathrm{m\,s^{-1}}$. The zero wind line is highlighted in bold solid contour lines, and westward (eastward) winds are indicated by dashed (solid) contour lines.

the model tops. This increase is most obvious above $\sim 55\,\mathrm{km}$ for ERA-Interim and above $\sim 45\,\mathrm{km}$ for JRA-55. Still, even though not very physical, the sponge layer effect seems to help simulate a more realistic SAO (Polichtchouk et al., 2017). Switching off the sponge leads to stronger mesospheric eastward winds at the Equator.

5.4 Gravity wave driving of the SAO in MERRA-2

Analogously to ERA-Interim and JRA-55, Fig. 4d shows that the MERRA-2 gravity wave driving $\overline{X}_{GW}$ in the altitude region 45–55 km (around the stratopause) is prevalently directed eastward. Peak values of eastward gravity wave drag in the single years are about $7\,\mathrm{m\,s^{-1}\,d^{-1}}$ (see Fig. S11), i.e., stronger than in ERA-Interim and JRA-55 (see Figs. S8 and S9). Westward-directed gravity wave drag in the stratopause region is generally weaker with peak values of usually $\sim 2\,\mathrm{m\,s^{-1}\,d^{-1}}$.

In the stratosphere, the QBO westward and eastward phases are usually stacked, and, since the zonal wind is usually stronger during QBO westward phases than during QBO eastward phases, the range of westward gravity wave phase speeds encountering critical level filtering is usually larger than the range of eastward phase speeds. This will lead to

an asymmetry of the gravity wave spectrum with a larger amount of eastward momentum flux entering the stratopause region and the mesosphere and, consequently, to the prevalently eastward driving of the stratopause SAO by gravity waves.

At times, the QBO eastward and westward phases are not perfectly stacked, resulting in less pronounced asymmetric wave filtering by the QBO. This is the case, for example, during April to June 2006 and April to June 2013. During these periods we find also relatively strong westward-directed gravity wave drag in the stratopause region (around 50 km altitude), and these enhancements seem to contribute to the formation of stronger downward-propagating SAO westward phases (see Fig. S11). Indications for the less asymmetric filtering of the gravity wave spectrum during 2006 were also found before from satellite observations (Ern et al., 2015).

Different from ERA-Interim and JRA-55, MERRA-2 assimilates MLS observations in the mesosphere. Further, the MERRA-2 model top is at higher altitudes, and increased damping is used only above $\sim 58\,\mathrm{km}$. Therefore, reasonable estimates of gravity wave drag should also be possible in the middle mesosphere. It is striking that in the alti-
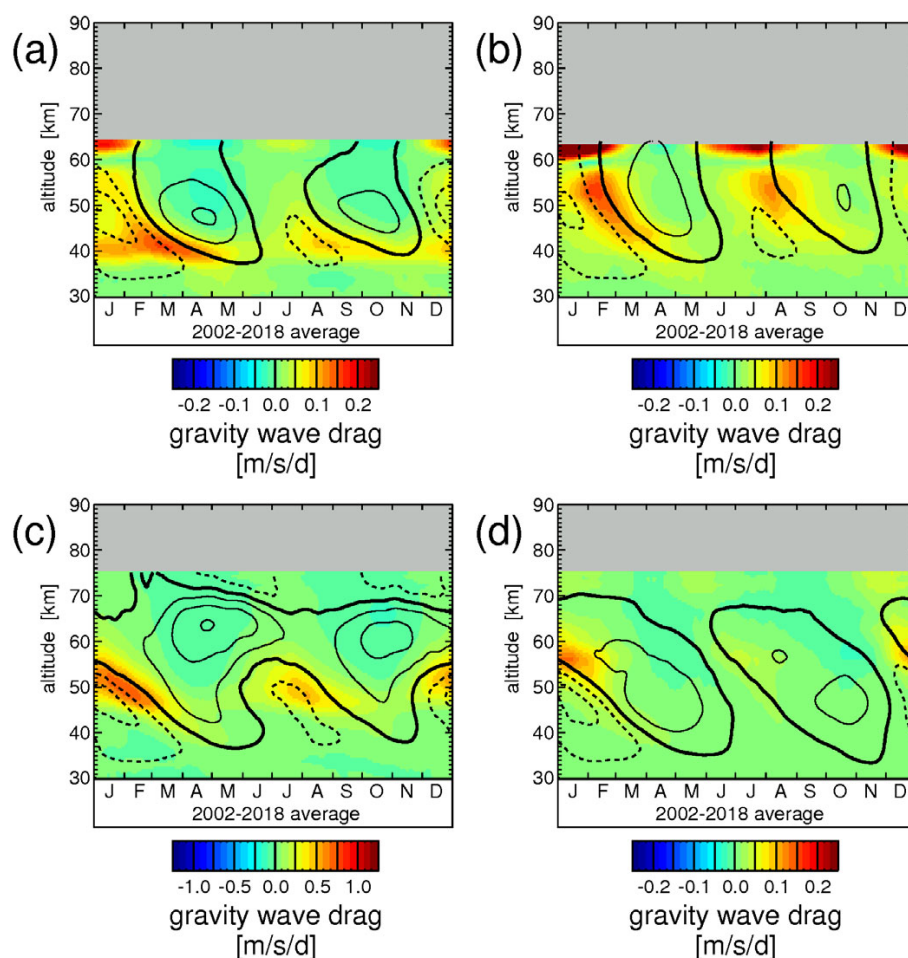
Figure 5. Same as Fig. 4 but for the zonal gravity wave drag $\overline{X}_{res}(k > 20)$ of model-resolved gravity waves at zonal wavenumbers exceeding $k = 20$.

tude range 55 km to somewhat above 65 km westward gravity wave drag is increased compared to the stratopause region, and sometimes is as strong as eastward gravity wave drag. In this altitude range, the westward gravity wave drag often contributes to the closure of the mesospheric SAO eastward wind jet at its top. Nevertheless, in this altitude range, the westward gravity wave drag is still, on average, only about half as strong as eastward gravity wave drag as shown from the multi-year average (Fig. 4d). At altitudes above ~ 65 km there is a sudden increase of eastward gravity wave drag in MERRA-2, which is likely unrealistic and related to damping in the sponge layer close to the model top, similarly as in ERA-Interim and JRA-55.

Note that MERRA-2 gravity wave drag is more strongly linked to vertical gradients of the background wind than is the case for ERA-Interim and JRA-55. Different from ERA-Interim and JRA-55, MERRA-2 uses a nonorographic gravity wave drag scheme. This scheme was additionally tuned to improve the QBO and the SAO in the tropics (Molod et al., 2015). Therefore, the strong link between gravity wave drag

and vertical gradients of the background wind could be an effect of the dedicated tuning of this gravity wave drag parameterization. This effect will be investigated in more detail in Sect. 7 based on satellite data and in Sect. 8 for the reanalyses.

5.5 Gravity wave driving of the SAO in ERA-5

Like ERA-Interim, JRA-55, and MERRA-2, the ERA-5 reanalysis shows an asymmetry between eastward and westward gravity wave drag in the stratopause region (Fig. 4c). However, peak values of eastward gravity wave drag are somewhat lower than those of MERRA-2. Furthermore, in the stratopause region, enhanced values of gravity wave drag are not as closely linked to zonal wind vertical gradients as it is the case for MERRA-2. This finding is surprising because, like MERRA-2, ERA-5 contains a nonorographic gravity wave drag scheme. Possibly, this difference is caused by different settings of the gravity wave drag schemes. For instance, enhanced gravity wave momentum fluxes were introduced in the tropics to improve the representation of the
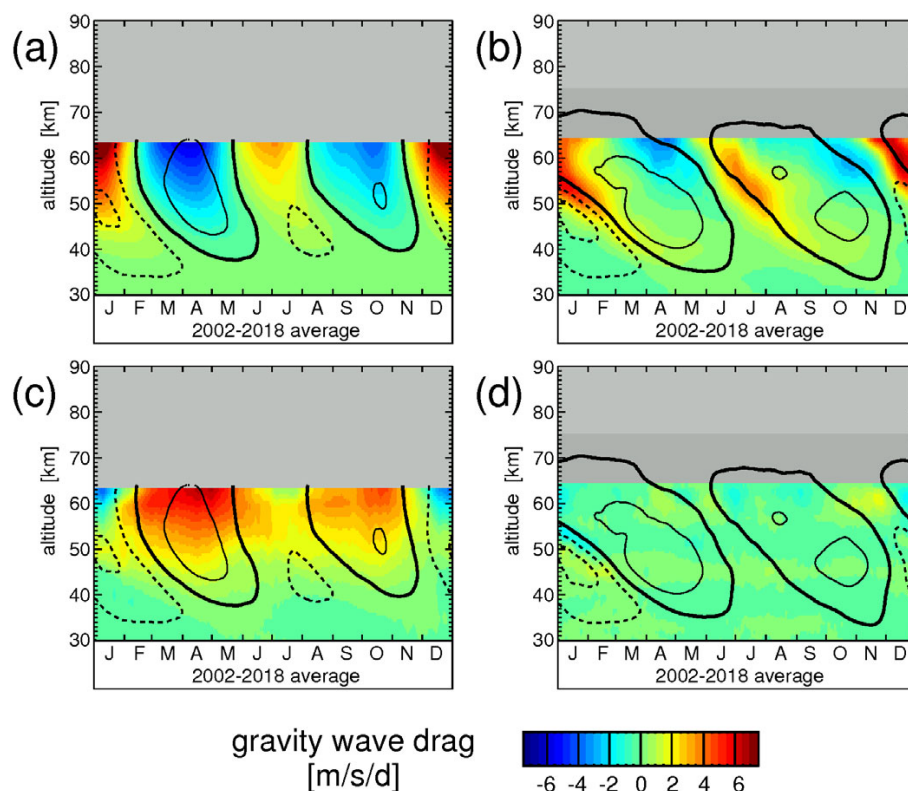
Figure 6. Typical seasonal variation of parameterized gravity wave drag $\overline{X}_{param}$ for the reanalyses **(a)** JRA-55 and **(b)** MERRA-2, as well as the gravity wave drag term $\overline{X}_{imbalance}$ for **(c)** JRA-55 and **(d)** MERRA-2. The term $\overline{X}_{imbalance}$ includes, for example, the model imbalance that is caused by data assimilation. Again, values are averages over 10° S–10° N and the time period 2002–2018, and contour lines of the respective wind data set are overlaid. Contour line increment is $20\,\mathrm{m\,s^{-1}}$. The zero wind line is highlighted in bold solid contour lines, and westward (eastward) winds are indicated by dashed (solid) contour lines.

QBO and the SAO in MERRA-2 (Molod et al., 2015), which is different in ERA-5.

The ERA-5 characteristics change at altitudes above about 65 km. At these altitudes also in ERA-5 enhanced gravity wave drag is closely linked to zonal wind vertical gradients, and strong westward-directed gravity wave drag contributes to the reversal of the mesospheric eastward-directed winds and the formation of the mesopause SAO, qualitatively consistent with MERRA-2. In MERRA-2, however, there is no clear wind reversal. Possibly, the sponge layer in MERRA-2 is stronger than that in ERA-5, preventing the formation of a clear MSAO. Still, there is some eastward-directed gravity wave drag near the model top in ERA-5 that seems to be related to the model sponge layer but that is much weaker than in MERRA-2.

6 Satellite observations of the SAO driving by gravity waves

One of the key parameters that is relevant for the interaction of gravity waves with the background flow is the vertical flux of gravity wave pseudomomentum ($\boldsymbol{F}_{ph}$), denoted in the fol-

lowing as "gravity wave momentum flux". The momentum flux of a gravity wave is given as

$$\boldsymbol{F}_{ph} = (F_{px}, F_{py}) = \varrho \left(1 - \frac{f^2}{\widehat{\omega}^2}\right) \left(\overline{u'w'}, \overline{v'w'}\right), \qquad (6)$$

with F_{px} and F_{py} being the gravity wave momentum flux in zonal and meridional directions, respectively; ϱ the atmospheric density; f the Coriolis frequency; $\widehat{\omega}$ the intrinsic frequency of the gravity wave; and (u', v', w') the vector of zonal, meridional, and vertical wind perturbations due to the gravity wave (e.g., Fritts and Alexander, 2003). If a gravity wave propagates conservatively, the momentum flux of a gravity wave stays constant. However, if a gravity wave dissipates while propagating upward, momentum flux is no longer conserved, and the gravity wave exerts drag on the background flow. This drag (X, Y) is related to the vertical gradient of momentum flux:

$$(X, Y) = -\frac{1}{\varrho} \frac{\partial \boldsymbol{F}_{ph}}{\partial z}, \qquad (7)$$

with X and Y being the gravity wave force in zonal and meridional direction, respectively, and z being the vertical direction. As will be explained in the next subsection, gravity

wave momentum flux can also be derived from temperature observations of satellite instruments.

6.1 Estimates of absolute gravity wave momentum fluxes and drag from SABER observations

6.1.1 Absolute momentum fluxes

For deriving gravity wave momentum fluxes from temperature altitude profiles observed by SABER, we make use of the method described in our previous studies (Ern et al., 2004, 2011, 2018). First, the atmospheric background temperature is estimated, separately for each altitude profile. This estimate consists of the zonal-average temperature profile. Further, 2D zonal-wavenumber/wave-frequency spectra are determined from SABER temperatures for a set of latitudes and altitudes. Based on these spectra, the contribution of global-scale waves is calculated at the location and time of each SABER observation. Both zonal-average profile and global-scale waves are removed from each altitude profile.

For our study, it is important that this 2D spectral approach is capable of effectively removing all global-scale waves that are important in the tropics, such as inertial instabilities in the tropical stratosphere and stratopause region (e.g., Rapp et al., 2018; Strube et al., 2020) and different equatorial wave modes in the stratosphere (e.g., Ern et al., 2008) and in the mesosphere and mesopause region (e.g., Garcia et al., 2005; Ern et al., 2009). In particular, Kelvin waves contribute significantly to the temperature variances in the tropics and are difficult to remove by other techniques, because they can have very short wave periods, and their vertical wavelengths are in the same range as that of small-scale gravity waves. Each altitude profile is additionally high-pass filtered to remove fluctuations of vertical wavelengths longer than about 25 km to focus on those gravity waves that are covered by our momentum flux analysis and to remove remnants of global-scale waves. Further, we explicitly remove tides by removing offsets and quasi-stationary zonal wavenumbers of up to 4, separately for ascending and descending orbit parts of SABER. In this way, we cover major tidal modes, such as the diurnal westward zonal wavenumber 1 (DW1), the semidiurnal westward zonal wavenumber 2 (SW2), and the diurnal eastward zonal wavenumber 3 (DE3). The final result of this procedure are altitude profiles of temperature fluctuations that can be attributed to small-scale gravity waves.

As introduced by Preusse et al. (2002), for each altitude profile the amplitude, vertical wavelength λ_z and the phase of the strongest wave component are determined in sliding 10 km vertical windows. Provided there is a close enough spacing in space and time, the gravity wave horizontal wavelength parallel to the satellite measurement track ($\lambda_{h,AT}$) can be estimated from pairs of consecutive altitude profiles if the same wave is observed with both profiles of a pair. To make sure that the same wave is observed in both profiles of a pair, a vertical wavelength threshold is introduced, and

we assume that the same wave is observed if λ_z differs between the two profiles by not more than 40 %. Pairs with non-matching vertical wavelengths are discarded. This omission of pairs does not introduce significant biases in distributions of gravity wave squared amplitudes (e.g., Ern et al., 2018). Therefore, the selected pairs should be representative of the whole distribution of gravity waves.

Taking $\lambda_{h,AT}$ as a proxy for the true horizontal wavelength λ_h of a gravity wave, absolute values of gravity wave momentum flux F_{ph} can be estimated:

$$F_{ph} = \frac{1}{2}\varrho\left(\frac{g}{N}\right)^2\frac{\lambda_z}{\lambda_h}\left(\frac{\widehat{T}}{T}\right)^2, \tag{8}$$

with g being the gravity acceleration, N the buoyancy frequency, T the background temperature, and $\widehat{T}$ the gravity wave temperature amplitude (see also Ern et al., 2004).

Generally, the use of along-track gravity wave horizontal wavenumbers $k_{h,AT} = 2\pi/\lambda_{h,AT}$ as a proxy for the true gravity wave horizontal wavenumbers $k_h = 2\pi/\lambda_h$ will lead to a low bias of SABER momentum fluxes (the momentum flux is proportional to the horizontal wavenumber). This is the case because $k_{h,AT}$ will always underestimate k_h (see also, for example Preusse et al., 2009; Alexander, 2015; Ern et al., 2017, 2018, or Song et al., 2018). In the tropics, the measurement tracks of satellites in low Earth orbit are usually oriented close to north–south, while the wave vectors of gravity waves should be oriented close to east–west, which will lead to even increased errors and stronger low biases of momentum fluxes in the tropics.

This effect has roughly been estimated by Ern et al. (2017) using observations of the Atmospheric Infrared Sounder (AIRS) satellite instrument. Because AIRS provides 3D temperature observations, it is possible to determine from AIRS observations true gravity wave horizontal wavenumbers, as well as along-track gravity wave horizontal wavenumbers. This opportunity has been taken by Ern et al. (2017) to compare true and along-track gravity wave horizontal wavenumbers: AIRS observations indicate an underestimation of the along-track wavenumber (corresponding to an underestimation of momentum fluxes) by a factor between 1.5 and somewhat above 2.

In addition, for SABER there will be aliasing effects (undersampling of observed gravity waves) and effects of the instrument sensitivity function of limb sounding satellite instruments (see also, for example Preusse et al., 2002), which should both lead to an even stronger underestimation of gravity wave momentum fluxes. The approximate SABER sensitivity function is given in Ern et al. (2018), and a comprehensive discussion of the observational filter of infrared limb sounders is given in Trinh et al. (2015). As was estimated by Ern et al. (2004) overall errors of F_{ph} are large, at least a factor of 2, and F_{ph} is likely strongly biased low.

6.1.2 A proxy for absolute gravity wave drag (SABER MFz-proxy-|GWD|)

Using the vertical gradient of absolute gravity wave momentum flux, a proxy of the absolute gravity wave forcing XY on the background flow can be estimated:

$$XY = -\frac{1}{\varrho}\frac{\partial F_{\mathrm{ph}}}{\partial z}. \tag{9}$$

In the following, this proxy will be called "SABER MFz-proxy-|GWD|".

A strong limitation is that, like for absolute gravity wave momentum fluxes, no directional information is available for the SABER MFz-proxy-|GWD|. Without further criteria being met, net gravity wave drag could be even zero due to cancellation effects, while SABER MFz-proxy-|GWD| may result in substantial drag.

However, if predominately gravity waves of one preference propagation direction dissipate, the vertical gradient of absolute gravity wave momentum flux is dominated by momentum loss in that direction, and the results are meaningful. This will be the case in two scenarios: first, in a strong vertical gradient of the background wind close to a wind reversal, gravity waves intrinsically propagating opposite to the wind are refracted to shorter vertical wavelengths and dissipate. The corresponding momentum transfer will mainly act to further decelerate the jet and facilitate the wind reversal. Second, if gravity waves dissipate that have already a strong preference direction, e.g., by filtering at altitudes below, the resulting drag will act in this preference direction. In these two cases cancellation effects due to dissipation of gravity waves of different propagation direction are relatively low, and SABER MFz-proxy-|GWD| can give information about the relative variations of absolute net gravity wave drag. For a further discussion, please see Warner et al. (2005) and Ern et al. (2011). And for previous applications of SABER MFz-proxy-|GWD|, please see, for example, Ern et al. (2013, 2014, 2015, 2016).

Of course, the same low biases and observational limitations as mentioned in Sect. 6.1.1 for absolute gravity wave momentum fluxes apply, which means that the magnitude of the SABER MFz-proxy-|GWD| is highly uncertain, and it is likely underestimated in the cases when the SABER MFz-proxy-|GWD| provides meaningful information.

Similarly to Ern et al. (2015), our data sets of SABER absolute gravity wave momentum fluxes and of SABER MFz-proxy-|GWD| are averages over 7 d with a step of 3 d; i.e., the time windows used for averaging are overlapping. In the following, we will discuss the interaction of the observed gravity waves with the background winds in the tropics.

6.2 Effect of the background winds on SABER gravity wave momentum fluxes

First, we investigate how SABER absolute gravity wave momentum fluxes are modulated by the background winds. Figure 7a shows the *typical year* of SABER absolute momentum fluxes. Values were obtained by averaging over the years 2002 until 2018 and over the latitude band 10° S–10° N. We also average over data from ascending and descending parts of the satellite orbit to reduce the effect of tides. Distributions for the single years 2002–2018 are shown in Fig. S20. Contour lines represent the combined data set of zonal winds from ERA-Interim, SABER quasi-geostrophic winds, and TIDI direct wind observations (E/S/T-winds), as presented in Fig. 3b.

Figure 7a shows that absolute gravity wave momentum flux in the stratopause region and in the middle mesosphere is usually strongest during periods of westward winds. This finding is consistent with the results obtained for the SSAO by Ern et al. (2015) and indicates that, due to the selective filtering of the gravity wave spectrum by the QBO in the stratosphere, the gravity wave spectrum in the stratopause region and in the middle mesosphere is dominated by gravity waves of eastward-directed phase speeds. An overall decrease of momentum fluxes with altitude shows that gravity waves dissipate gradually with increasing altitude. In addition to this overall decrease, momentum fluxes decrease more strongly in zones of eastward (positive) wind shear, which indicates that gravity waves interact with the SAO winds in the stratopause region and middle mesosphere and contribute to the driving of the SAO. This effect will be investigated in more detail in Sect. 6.3 based on the SABER MFz-proxy-|GWD|. In the upper mesosphere and in the mesopause region, there is no such clear relationship between momentum fluxes and positive wind shear. This effect will also be discussed later in Sect. 6.3.

6.3 Interaction of the SABER MFz-proxy-|GWD| and the tropical zonal wind

Figure 7b shows the *typical year* of the SABER MFz-proxy-|GWD| obtained by averaging over the years 2002 until 2018. Again, values are averaged over the latitude band 10° S–10° N and over ascending and descending orbit data. Distributions for the single years 2002–2018 are shown in Fig. S21. Contour lines represent the zonal winds shown in Fig. 3b. From Fig. 7b we can see that the SABER MFz-proxy-|GWD| generally increases with height from close to zero at 30 km to around $20\,\mathrm{m\,s^{-1}\,d^{-1}}$ between 80 and 90 km. It has a local maximum around 50 km with peak values of about 1–$2\,\mathrm{m\,s^{-1}\,d^{-1}}$ and another local maximum between around 80 and 85 km with peak values of about $30\,\mathrm{m\,s^{-1}\,d^{-1}}$ during single years. Peak values are somewhat reduced for the *typical year*. The first maximum is likely related to the

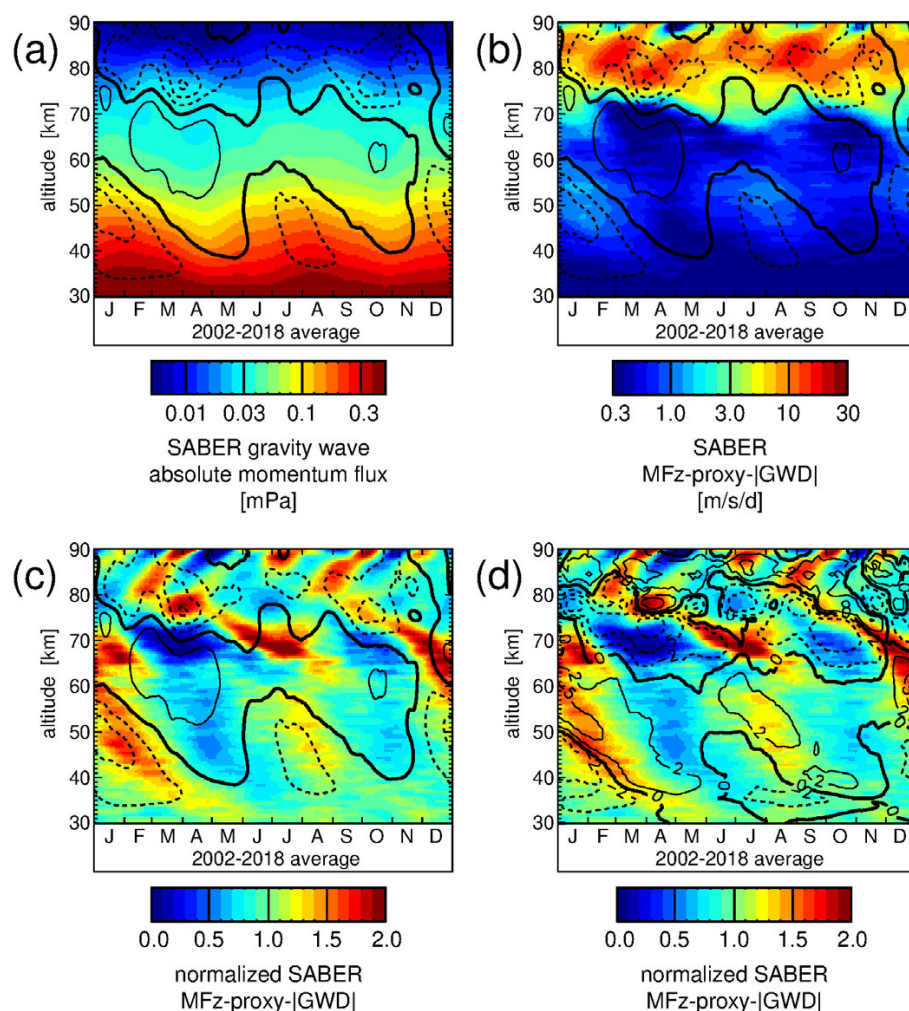**Figure 7.** Typical seasonal variation of **(a)** SABER absolute gravity wave momentum fluxes, **(b)** SABER MFz-proxy-|GWD|, and **(c)** SABER MFz-proxy-|GWD| normalized by the altitude-dependent annual means. Overlaid in **(a–c)** are contour lines of the E/S/T-wind data set. Contour line increment is $20\,\mathrm{m\,s^{-1}}$. The zero wind line is highlighted in bold solid contour lines, and westward (eastward) winds are indicated by dashed (solid) contour lines. In addition, **(d)** shows the same as **(c)** but overlaid contour lines are the vertical gradient $\mathrm{d}u/\mathrm{d}z$ of the E/S/T-winds. Contour lines are at $0, \pm 2, \pm 5$, and $\pm 10\,\mathrm{m\,s^{-1}\,km^{-1}}$. Westward (meaning negative) gradients are indicated by dashed contour lines.

SSAO, while the second maximum is likely related to the MSAO.

6.3.1 The SSAO and the SAO in the middle mesosphere

In the stratopause region, peak values of SABER MFz-proxy-|GWD| are seen mainly during eastward wind shear, while values are much reduced during westward wind shear, indicating that gravity wave drag is mainly directed eastward and contributes to the driving of the SAO eastward wind phases. This finding is consistent with the HIRDLS observations discussed by Ern et al. (2015) and becomes even clearer when looking at Fig. 7c and d.

Figure 7c and d shows the *typical year* of SABER MFz-proxy-|GWD| normalized by the altitude-dependent annual mean. These normalized distributions are calculated for each year 2002 until 2018 (see Figs. S22 and S23) and then averaged to obtain the *typical year*. Overlaid contour lines in Fig. 7c represent the zonal winds shown in Fig. 3b, while the contour lines in Fig. 7d represent the vertical gradient of this zonal wind. Figure 7c and d reveal that SABER MFz-proxy-|GWD| is enhanced mainly during eastward wind shear, not only in the stratopause region but also in the whole altitude range of about 40–70 km.

Parts of the gravity wave spectrum, particularly those of low ground-based phase speeds, have encountered critical levels already at lower altitudes by the QBO (see Ern et al., 2014, 2015) and cannot contribute to the SAO driving. Therefore, an enhancement of gravity wave drag mainly during eastward zonal wind shear does not necessarily mean that

critical level filtering of gravity waves is the only dominant process. Another effect of vertical wind shear, in addition to the formation of critical levels, is a reduction of intrinsic phase speeds for parts of the gravity wave spectrum and, thus, a reduction of gravity wave saturation amplitudes for this part of the spectrum. This means that wave saturation apart from critical levels, i.e., saturation of high ground-based phase speed gravity waves, can also play an important role in the stratopause region and even more at higher altitudes. Indications for the importance of saturation of high-phase-speed gravity waves for the SSAO were indeed found by Ern et al. (2015) by investigating gravity wave momentum flux spectra observed from satellite.

In the stratopause region the magnitudes of SABER MFz-proxy-|GWD| (peak values of around $1–2\,\mathrm{m\,s^{-1}\,d^{-1}}$) are similar or even stronger than those obtained by model simulations of the SSAO (e.g., Richter and Garcia, 2006; Osprey et al., 2010; Peña-Ortiz et al., 2010; Smith et al., 2020) and similar to values derived from Rayleigh lidar observations (Deepa et al., 2006; Antonita et al., 2007). Comparison with the reanalyses gives a somewhat different picture: SABER gravity wave drag is usually weaker than peak values of eastward gravity wave drag of the four reanalyses considered in our study. For example, at around 50 km altitude peak values of eastward gravity wave drag in the multi-year averages are around 3 to $4\,\mathrm{m\,s^{-1}\,d^{-1}}$ for ERA-Interim (see Fig. 4a), 3 to $6\,\mathrm{m\,s^{-1}\,d^{-1}}$ for JRA-55 (see Fig. 4b, but values could be already affected by the model sponge layer), $\sim 2\,\mathrm{m\,s^{-1}\,d^{-1}}$ for ERA-5 (see Fig. 4c), and $\sim 3\,\mathrm{m\,s^{-1}\,d^{-1}}$ for MERRA-2 (see Fig. 4d).

Generally, observations cover only parts of the whole spectrum of gravity waves and should therefore underestimate gravity wave drag. An underestimation of the gravity wave drag derived from SABER observations would be expected for two reasons. First, SABER momentum fluxes are likely underestimated due to overestimation of derived horizontal wavelengths by undersampling of observed gravity waves (aliasing) and by adopting along-track wavelengths instead of the true horizontal wavelengths (see Ern et al., 2018, and references therein). Second, the SABER instrument is sensitive only to gravity waves of horizontal wavelengths longer than 100–200 km and does therefore not cover the whole spectrum of gravity waves. In particular, it is indicated that short-horizontal-wavelength convectively generated gravity waves that cannot be seen by SABER contribute significantly to the driving of the SSAO (e.g., Beres et al., 2005; Kang et al., 2018). For further discussion regarding the observational filter of the instrument, please see Trinh et al. (2015).

In their study, Smith et al. (2020) conclude that free-running models would have difficulties to simulate a realistic SSAO because of insufficient gravity wave forcing. This conclusion is supported by the fact that the magnitude of gravity wave drag of free-running global models is similar to the magnitude of SABER MFz-proxy-|GWD| (that should be bi-

ased low by observational filter effects) and lower than the magnitude of total gravity wave drag in reanalyses.

6.3.2 Upper mesosphere: the MSAO

In the upper mesosphere, at altitudes between about ~ 75 and 80 km, the clear relationship between eastward wind shear and SABER MFz-proxy-|GWD| apparently does not hold any longer (see Fig. 7c and d). This is expected because the asymmetric wind filtering effect of the gravity wave spectrum induced by the QBO in the stratosphere should gradually fade out. Instead, the wind filtering in the stratopause region and the middle mesosphere should become more relevant.

This is supported by the fact that the MSAO is approximately in anti-phase with the SAO at the stratopause and in the middle mesosphere. It is believed that this anti-phase relationship is caused by the dissipation of gravity waves that are selectively filtered by the winds in the middle mesosphere. Gravity waves that have phase speeds opposite to the prevailing wind direction in the stratopause region and the middle mesosphere, consequently, have high intrinsic phase speeds and, thus, high saturation amplitudes (see also Fritts, 1984; Ern et al., 2015, and references therein). When reaching the upper mesosphere, these waves saturate and contribute to the wind reversal, resulting in the observed anti-correlation of SAO winds in the middle and the upper mesosphere. This means that winds in the upper mesosphere are westward when they are eastward in the middle mesosphere and vice versa. Accordingly, in the upper mesosphere gravity waves are expected to contribute both to the MSAO eastward and the MSAO westward winds.

Interestingly, as shown by the SPARC zonal wind climatology, the downward propagation with time of the MSAO eastward and westward wind phases is much slower than the downward propagation of the eastward wind phase of the SSAO and the SAO in the middle mesosphere. Therefore, the characteristics of the gravity wave forcing should also be different in these two altitude ranges. This will be investigated in more detail in Sect. 7.

Peak values of SABER MFz-proxy-|GWD| in the altitude range of 75–80 km are about $20–30\,\mathrm{m\,s^{-1}\,d^{-1}}$ (see Figs. 7b and S21). As stated before, due to the SABER observational filter, these values are expected to likely be a lower estimate of the total gravity wave drag. Indeed, in the mesopause region, Lieberman et al. (2010) obtained gravity wave peak values of typically around $100\,\mathrm{m\,s^{-1}\,d^{-1}}$, estimated as residual drag from the momentum budget using TIMED observations of SABER and TIDI. However, similarly as for the simulation of the stratopause SAO, gravity wave drag peak values of model simulations are much weaker. For example, Richter and Garcia (2006) or Peña-Ortiz et al. (2010) obtained peak values of gravity wave drag of only around $10–20\,\mathrm{m\,s^{-1}\,d^{-1}}$ in their simulations of the SAO in the altitude range 75–85 km.

6.3.3 The region above the MSAO

Also at altitudes above 80 km, there is no clear relationship between eastward wind shear and SABER MFz-proxy-|GWD|. Moreover, compared to the altitude range 30–80 km, there is a structural change in the distribution of SABER MFz-proxy-|GWD| (see Fig. 7c and d).

In the whole lower altitude regime 30–80 km, we find downward propagation of SABER MFz-proxy-|GWD| enhancements with time. At altitudes of ~ 30–75 km, this downward propagation is relatively steep and related to the zones of eastward-directed SAO wind shear. At altitudes of 75–80 km, we still find downward propagation, although much slower, and they are seemingly related to the downward propagation rate of the SAO wind phases (see Fig. 3b).

Conversely, in the upper altitude regime above 80 km, enhancements of SABER MFz-proxy-|GWD| propagate *upward* with time. These variations are obviously not directly related to the SAO winds but to the variations that are caused by the varying local solar time of SABER observations. The variations of SABER MFz-proxy-|GWD| at altitudes above ~ 80 km are caused by tides that are sampled at different local solar times while the TIMED satellite orbit precesses. For upward-propagating tides, the phase propagation is downward with time (e.g., Smith, 2012; Sridharan, 2019). However, due to orbit precession of the TIMED satellite, the SABER sampling gradually shifts to earlier local solar times, as shown in Fig. S1. This leads to an apparent upward phase propagation with time of observed tides and, accordingly, to the observed apparent upward propagation of gravity wave drag maxima, because gravity wave drag should be directly linked with the wind shear induced by the tides.

At high altitudes, an increasing influence of tides on the distribution of gravity waves would also be expected: the gravity wave momentum flux spectrum is strongly filtered by the QBO, the SSAO, and the SAO in the middle mesosphere. Consequently, not much momentum flux is still available for driving the MSAO in more than a narrow altitude layer. Also previous findings show that the MSAO occurs only in a narrow layer, and at some point the effect of tides starts to dominate over the effect of the SAO. For instance, Fig. 30 in Baldwin et al. (2001) shows that the MSAO in the upper mesosphere has a sharp amplitude peak of $30 \, \mathrm{m \, s^{-1}}$ at 80 km altitude. The MSAO amplitude drops below $\sim 10 \, \mathrm{m \, s^{-1}}$ already below 90 km. Simultaneously, the amplitude of tides increases with altitude. For example, Fritts et al. (1997) found amplitudes of 5–10 m s^{-1} below 75 km, increasing to about 20 m s^{-1} at 90 km for diurnal tides observed by radar near the Equator during August 1994. These values are roughly in agreement with simulations of the Canadian Middle Atmosphere Model (CMAM) (McLandress et al., 2002). Based on these findings, it would be expected that in the altitude range 80–90 km there should be a transition between a regime that is mainly dominated by the MSAO around 80 km and another regime that is increasingly dominated by tides at higher altitudes. Worthy of remark is that this is also reflected in the observed distribution of SABER MFz-proxy-|GWD|.

7 Correlation between SABER MFz-proxy-|GWD| and tropical zonal wind

Next, we carry out a correlation analysis in order to quantify the robustness of the interaction between SABER MFz-proxy-|GWD| and tropical zonal background wind. To do so, we calculate the temporal correlation between SABER MFz-proxy-|GWD| and the vertical gradient of the background zonal wind as well as the temporal correlation between SABER MFz-proxy-|GWD| and absolute values of the zonal background wind. These correlations are calculated for fixed altitudes, separately for each given year of the 2002–2018 period, for the distributions that are obtained by averaging over these years and for the complete time series as a whole.

Figure 8 shows 2002–2018 averages of SABER MFz-proxy-|GWD| with zonal wind contour lines (first column), normalized SABER MFz-proxy-|GWD| with contour lines of zonal wind vertical gradients (second column), correlation coefficients between SABER MFz-proxy-|GWD| and du/dz (third column), and correlation coefficients between SABER MFz-proxy-|GWD| and $|u|$ (fourth column). In order to find out whether the results are robust and insensitive to details of a wind data set considered, the correlation analysis is carried out for different wind data sets.

Given the strong interannual variability of the SAO, it is most important that existing correlations hold for the majority of single years, and this is why in Figs. 8 and 9 we show the correlations for each year of the 2002–2018 period. For completeness, also the correlations are shown for the 2002–2018 average distribution, as well as for the complete 2002–2018 time series as a whole. These correlations might, however, differ somewhat from the correlations of the single years. For example, the correlations for the average might be affected by strong outlier years or compensation effects, and also the correlation over the whole data set might be affected by strong outlier years (although in a different way).

7.1 Correlation between SABER MFz-proxy-|GWD| and du/dz

From theoretical considerations (e.g., Hamilton and Mahlmann, 1988; Dunkerton and Delisi, 1997) from first satellite observations of the gravity wave driving of the SAO in the stratopause region (Ern et al., 2015) and from the findings in Sect. 6.3, we expect that in a certain altitude range gravity waves mainly contribute to the driving of the SAO eastward phases and their downward propagation with time. For this altitude range, it is expected that gravity wave drag should mainly act during eastward wind shear.
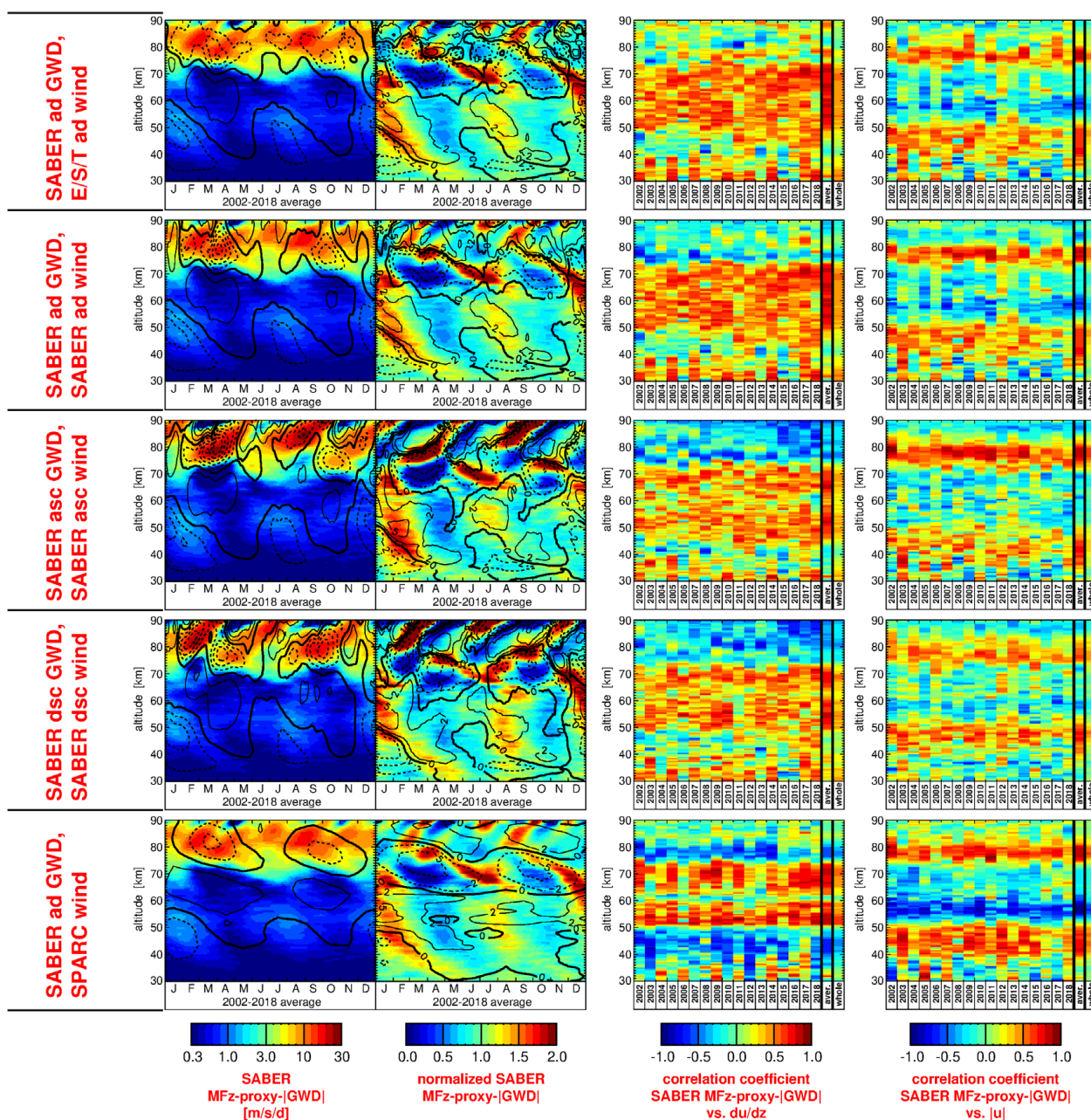
Figure 8. Left column: the SABER MFz-proxy-|GWD| (a proxy for absolute gravity wave drag) averaged over 10° S–10° N and the years 2002–2018, overlaid with zonal wind contour lines of different zonal wind data sets averaged over the same latitudes and period. Second column: same as left column but for normalized SABER MFz-proxy-|GWD| overlaid with contour lines of zonal wind vertical gradients. Third column: temporal correlations between SABER MFz-proxy-|GWD| and zonal wind vertical gradients, separately for each year, for the multi-year averages, and for the whole time series. Right column: same as third column but for the correlation between SABER MFz-proxy-|GWD| and zonal wind absolute values. The different rows are (from top to bottom) for (1) the merged ERA-Interim, SABER and TIDI data set as described in Sect. 4.2.3 averaged over ascending and descending orbit legs; (2) ERA-Interim and SABER winds merged, similarly as for MLS in Sect. 4.2.2, averaged over ascending and descending orbit legs (i.e., SABER geostrophic winds are used also above 75 km); (3) same as (2) but only for ascending orbit legs; (4) same as (2) but only for descending orbit legs; and (5) SPARC climatology winds (same wind used for each year). For zonal winds, contour line increment is $20 \, \text{m s}^{-1}$. The zero wind line is highlighted in bold solid contour lines, and westward (eastward) winds are indicated by dashed (solid) contour lines.
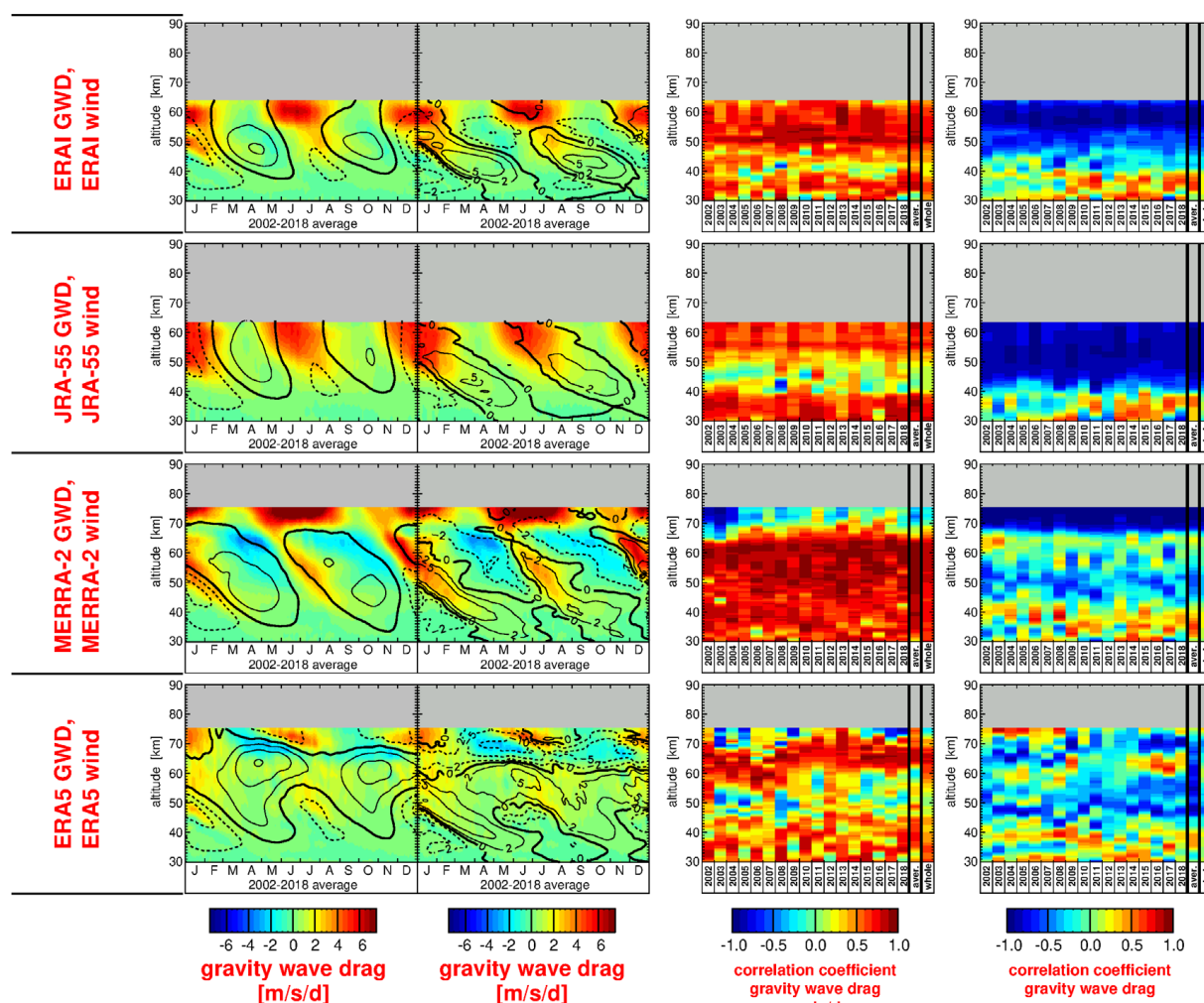
Figure 9. Left column: gravity wave drag (in $m\,s^{-1}\,d^{-1}$) derived from the four reanalyses considered in this study, averaged over the latitude band 10° S–10° N and the years 2002–2018, overlaid with contour lines of the corresponding zonal winds averaged over the same latitudes and time period. Second column: same as left column but contour lines are the vertical gradient of the zonal wind. Third column: temporal correlations between reanalysis gravity wave drag and zonal wind vertical gradients, separately for each year, for the averages over the different years, and for the time series as a whole. Right column: temporal correlations between reanalysis gravity wave drag and zonal wind, separately for each year, for the averages over the different years, and for the time series as a whole. The different rows are (from top to bottom) for (1) ERA-Interim, (2) JRA-55, (3) MERRA-2, and (4) ERA-5. For zonal winds, contour line increment is $20\,m\,s^{-1}$. The zero wind line is highlighted in bold solid contour lines, and westward (eastward) winds are indicated by dashed (solid) contour lines.

To find out in which altitude range this is the case, we calculated for each year separately the temporal correlation between SABER MFz-proxy-|GWD| and du/dz. Since SABER MFz-proxy-|GWD| can attain only positive values, some care has to be taken when interpreting these results. If a correlation coefficient is positive, this means that in a given year, at the altitude considered, the gravity wave forcing mainly takes place during eastward wind shear, and the forcing is very likely eastward. Similarly, if the correlation coefficient is negative, the gravity wave forcing mainly takes place during westward wind shear, and the forcing is very likely westward. If the correlation is close to zero, this means that either the relationship between gravity wave drag and

du/dz is random or eastward and westward forcing could be similarly strong.

7.1.1 Stratosphere (QBO)

Figure 8, first row, shows the results for the combined data set of ERA-Interim, SABER, and TIDI winds, averaged over ascending and descending orbit data. In the stratosphere between about 30 and 40 km, there is an alternating pattern of strong positive and weak correlations, which is likely not an effect of the SAO. In this altitude range the QBO is the dominant mode of tropical wind variability. It has been shown by Ern et al. (2014) that HIRDLS and SABER absolute grav-

ity wave drag proxies are stronger during eastward-directed QBO wind shear. Although the 10 km vertical window used in our study is relatively coarse and will often average over the stacked zones of eastward- and westward-directed QBO wind shear, this asymmetry can lead to the observed alternating pattern of correlations. Since the QBO averages out in the 2002–2018 multi-year average, correlations for the average distributions are generally weak at altitudes below about 45 km; the same holds for the correlations over the complete 2002–2018 time series as a whole. Similar alternating patterns are also found for all other wind data sets presented in Fig. 8 (and in Fig. S24) that contain the QBO. Even for the correlation between the SPARC zonal wind climatology and SABER MFz-proxy-|GWD| an alternating pattern can be found in the stratosphere. However, this pattern is different, because the QBO signal is only contained in the SABER MFz-proxy-|GWD| but not in the winds, as the same wind climatology is assumed for all years.

7.1.2 Stratopause region (SSAO) and middle mesosphere

In all panels of the third column in Fig. 8, starting from about 45 km upward, correlation coefficients are mostly strongly positive for the quasi-geostrophic data sets based on the SABER observations (Fig. 8, first to fourth row, and Fig. S24, first two rows), independently of the treatment of ascending and descending orbit data. This is also the case if MLS quasi-geostrophic winds (Fig. S24, bottom row) or the SPARC wind climatology (Fig. 8, bottom row) are used as background winds.

For the SABER quasi-geostrophic wind data sets (Fig. 8, rows 1–4), the altitude range of positive correlations is from about 45 to 75–80 km, indicating that in this altitude range gravity waves mainly contribute to the driving of the eastward SAO phase. Interestingly, for the SPARC wind climatology (Fig. 8, bottom row), the altitude range of positive correlations starts only at ~ 50 km, which is somewhat higher than for all other data sets. A possible reason could be that for the SPARC climatology the SAO in the stratopause is less pronounced than for the other data sets, and it is somewhat shifted in its phase. However, as in the other data sets, the upper edge of the positive correlations with $\mathrm{d}u/\mathrm{d}z$ is at about 75 km. At around 60 km altitude the correlation between SPARC zonal wind vertical gradients and SABER gravity wave drag is somewhat weaker, possibly because this altitude range is interpolated in the SPARC climatology and might be less reliable (see Swinbank and Ortland, 2003).

7.1.3 Upper mesosphere: MSAO and effect of tides

At altitudes above about 75–80 km the positive correlation between the SABER MFz-proxy-|GWD| and $\mathrm{d}u/\mathrm{d}z$ no longer holds. For the MSAO, this means that the mechanisms of the gravity wave driving are somewhat different than at lower altitudes. This will be discussed in Sect. 7.2.

Above 80 km there is even an anti-correlation between SABER MFz-proxy-|GWD| and $\mathrm{d}u/\mathrm{d}z$ when the SABER quasi-geostrophic winds are used also in the whole altitude range above 75 km and separated into data from ascending and descending orbit legs (Fig. 8, third and fourth row). The fact that this effect occurs when ascending and descending data, i.e., different local solar times, are treated separately hints at an effect of tides.

There is even a phase shift by about 180°: maxima of SABER MFz-proxy-|GWD| from ascending-only data fall onto minima of SABER MFz-proxy-|GWD| from descending-only data and vice versa (Fig. 8, third and fourth rows, second column). A similar phase shift is seen in the ascending-only and descending-only quasi-geostrophic winds at altitudes above about 75–80 km (Fig. 8, third row, left, and fourth row, left).

Obviously, enhancements of absolute gravity wave drag are phase-locked with tidal winds and their vertical shear. This is not surprising because gravity waves can interact with global-scale waves (e.g., Holton, 1984; Smith, 2003; Matthias and Ern, 2018), and, in particular, tides as seen from model simulations (e.g., Mayr et al., 2001; England et al., 2006; Ortland and Alexander, 2006; Liu et al., 2014; Ribstein and Achatz, 2016) and observations (e.g., Fritts and Vincent, 1987; Preusse et al., 2001; Tang et al., 2014).

However, an in-depth investigation of the impact of tides on the gravity wave distribution is beyond the scope of this paper, and for an in-depth study direction-resolved observations of momentum fluxes would be very helpful. Still, because of the anti-phase relationship between ascending and descending data, we can assume that cancellation effects will take effect if ascending and descending data are averaged, and the contribution of the SAO should become more clearly visible. This cancellation should hold for both the zonal wind and the SABER MFz-proxy-|GWD|.

7.2 Correlation between SABER MFz-proxy-|GWD| and absolute zonal wind

So far we have mainly discussed the case of gravity wave forcings when a strong vertical wind shear coincides with enhancements of the SABER MFz-proxy-|GWD|. Under these conditions, it is likely that either critical level filtering of gravity waves takes place (background winds and ground-based phase speeds become equal for parts of the gravity wave spectrum) or the vertical gradient of the background wind leads to a reduction of intrinsic phase speeds for parts

of the gravity wave spectrum such that those waves saturate and dissipate.

Of course, wave saturation can also occur independent of gradients of the background wind. If a gravity wave propagates upward conservatively in a background of constant wind and temperature, its amplitude will grow exponentially due to the decrease of atmospheric density with altitude. Upon reaching the saturation amplitude, the gravity wave will break and dissipate (e.g., Fritts, 1984). This mechanism is assumed to cause the wind reversals of the midlatitude mesospheric wind jets in the mesopause region (e.g., Lindzen, 1981). It is expected that this mechanism should also be relevant for the driving of the MSAO, and it would explain the out-of-phase or anti-phase relationship with the SAO at lower altitudes (e.g., Dunkerton, 1982; Mengel et al., 1995), as well as the relatively slow downward propagation of the MSAO phases. While correlations between du/dz and absolute gravity wave drag can be explained by critical level filtering or by gravity wave saturation, it is difficult to explain correlations between the strength of the zonal wind and absolute gravity wave drag by processes other than a general saturation mechanism of gravity waves.

First indications for a relationship between the strength of the zonal wind and absolute gravity wave drag were found in Sect. 6.3.2 for certain altitude ranges. This will now be investigated in more detail. Because SABER MFz-proxy-|GWD| provides only absolute values, we will investigate in the following the correlation between *absolute values* of the zonal wind ($|u|$) and SABER MFz-proxy-|GWD|. A correlation analysis between SABER MFz-proxy-|GWD| and zonal wind, including its sign, would not make sense because correlations for situations where both positive and negative wind phases are driven by gravity wave dissipation (as would be expected for the MSAO) would be near-zero due to cancellation effects. Correlation coefficients for the relation between $|u|$ and SABER MFz-proxy-|GWD| are shown in the rightmost column of Fig. 8 in the same manner as before, i.e., for the different wind data sets, separately for each year, as well as for the multi-year average and the time series as a whole.

7.2.1　Altitudes below about 75 km

At altitudes below about 40 km the dominant mode of stratospheric variability in the tropics is the QBO. Indeed, there is some interannual variability due to the QBO in all panels of the rightmost column of Fig. 8. However, as mentioned before, this QBO signal should be only spurious because the 10 km vertical window of our SABER momentum flux analysis will average out much of the QBO signal.

In the altitude range from about 40 to 50 km we find a positive correlation between SABER MFz-proxy-|GWD| and $|u|$ for all wind data sets. One reason is the asymmetry of the SAO in this altitude region, so most of the positive wind gradient falls into the negative (meaning westward) phase of the SAO, which is stronger than the eastward phase. An-

other reason is that part of the gravity wave driving, particularly during the first SAO westward phase of the year, takes place not only during eastward wind shear but also around the line of zero wind shear, i.e., around maximum westward winds (see Fig. 8, second column). As was argued by Ern et al. (2015), this effect could be caused by gravity waves of eastward-directed phase speeds that saturate before the vertical gradient, du/dz, of the background wind becomes positive. This is supported by the fact that for this case most of the momentum flux reduction happens at high gravity wave intrinsic phase speeds (Ern et al., 2015). Further, during the first stratopause SAO westward phase for a given year, the gravity wave drag estimated from the reanalyses is mostly eastward (see Fig. 4a–d). Still, as can be seen from Fig. 4a–d, sometimes the net forcing can also be westward.

In the altitude range from about 50 to 75 km, correlations are usually weak (floating around zero) or even negative. Strongest negative correlations are found for the SPARC zonal wind climatology (Fig. 8, lower right panel) at altitudes between 50 and 60 km, indicating that for the SPARC climatology the timing of the SAO in the lower mesosphere is somewhat different from the other data sets. Overall, the weak or negative correlations confirm that in the altitude range of 50 to 75 km the SAO gravity wave driving indeed mainly happens during eastward wind shear.

7.2.2　Upper mesosphere and mesopause region

In the upper mesosphere, at altitudes above 75 km, the correlation between SABER MFz-proxy-|GWD| and du/dz is usually weak, consistent with our findings in Sect. 7.1.3. Remarkably, there is a strong positive correlation between SABER MFz-proxy-|GWD| and $|u|$ in the altitude region of about 75 to 85 km for most of the wind data sets presented in Figs. 8 and S24. This correlation holds for each given year, for the average year of the 2002–2018 period, as well as for the 2002–2018 time series as a whole. The only exception is the data set of MLS winds (see Fig. S24, third row, rightmost column), which could be due to an altitude-dependent bias caused by sampling tides always at the same phases.

Apart from this exception, good correspondence between SABER MFz-proxy-|GWD| and absolute zonal wind is found for the data sets that are based on SABER quasi-geostrophic winds merged with TIDI direct wind observations (Fig. 8, first row, rightmost column; Fig. S24, first two rows, rightmost column) and for the data sets that (in this altitude region) are based solely on SABER quasi-geostrophic winds (Fig. 8, rows two to four, rightmost column). Note that this correlation holds for ascending-only data, for descending-only data, as well as for the averages of ascending and descending data. Further, it is remarkable that the same altitude range of positive correlations is also found for the SPARC climatology (Fig. 8, bottom row, rightmost column).

At altitudes above 85 km, in the mesopause region, correlations fluctuate around zero or are negative again. As stated in Sect. 7.1.3, this altitude region is dominated by tides, and SABER MFz-proxy-|GWD| seems to be phase-locked with the tidal component of the SABER quasi-geostrophic winds. An interpretation of these results, however, is difficult and beyond the scope of this study.

Overall, the positive correlations between SABER MFz-proxy-|GWD| and absolute zonal wind speed at altitudes 75–85 km support the mechanism proposed by previous studies (e.g., Dunkerton, 1982; Mengel et al., 1995; Burrage et al., 1996) that in this altitude range selectively filtered gravity waves saturate and directly contribute to the formation of the MSAO westward and eastward phases. The direction of the wave forcing is given by the selective filtering of gravity waves at altitudes below, leading to the observed anti-correlation of the MSAO (i.e., the SAO in the upper mesosphere) and the SAO in the middle mesosphere. The wave saturation seems to take place independent of zonal wind vertical gradients, which means that gravity waves of phase speeds much higher than the background wind are involved.

The saturation amplitudes of high-phase-speed gravity waves are not much influenced by the background wind and its variation. Consequently, the saturation altitude (the altitude where the waves exert their drag) will not be as closely tied to a wind shear zone as is the case for the QBO and the SAO at lower altitudes. Still, the dissipation of high-phase-speed gravity waves with a directional preference can lead to a reversal and strengthening of the wind by inducing a *temporal wind tendency*, which is different from the dissipation mechanism that leads to a strengthening of *vertical wind shear* and eventually to a downward propagation of the shear zone. The temporal wind tendency will lead to a wind reversal and wind strengthening at the same altitude where the drag is exerted. Therefore, enhanced gravity wave drag should be observed at the same altitude as the reversed wind jet and lead to a correlation between SABER MFz-proxy-|GWD| and (absolute) wind speed. This mechanism seems to be relevant for the driving of the MSAO, and it would explain why there is no strong downward propagation of the MSAO eastward and westward wind phases with time. For an in-depth understanding of this mechanism, however, more detailed model studies would be needed.

8 Correlation between reanalysis gravity wave drag and zonal wind

Next, we will investigate whether the gravity wave drag expected from the reanalyses exhibits similar characteristic patterns that are consistent with the SABER observations. Similarly as in Fig. 8, Fig. 9 shows for the four reanalyses, averaged over the period 2002–2018 and latitudes 10° S–10° N, gravity wave drag overlaid with zonal wind contour lines (Fig. 9, left column) and gravity wave drag overlaid with contour lines of the zonal wind vertical gradient du/dz (Fig. 9, second column). Further shown are for each altitude temporal correlations between gravity wave drag and the zonal wind vertical gradient (Fig. 9, third column) and gravity wave drag and zonal wind including direction (Fig. 9, right column). Unlike for SABER MFz-proxy-|GWD|, the latter makes sense for the reanalyses, because the gravity wave drag derived from the reanalyses has directionality. Again, correlations are shown for each year, for the 2002–2018 average distributions, and for the complete 2002–2018 time series as a whole.

8.1 ERA-Interim

As can be seen from Fig. 9, first row, third column, ERA-Interim gravity wave drag is generally positively correlated with du/dz with some interannual variation at altitudes below about 45 km that may be related to the QBO. This is consistent with our findings for SABER gravity wave drag (see Fig. 8). However, for ERA-Interim there is a strong anti-correlation between zonal wind and gravity wave drag at altitudes above ∼ 45 km (Fig. 9, first row, right column). This correlation is not observed for SABER MFz-proxy-|GWD| and should be an effect of the model sponge layer near the model top. Therefore, patterns of ERA-Interim gravity wave drag are likely not very realistic at altitudes above 45 km.

8.2 JRA-55

For JRA-55, at altitudes below ∼ 45 km the correlation between gravity wave drag and du/dz is much stronger than for ERA-Interim or for SABER. This indicates that details in the gravity wave driving of the QBO are different in JRA-55 (see Fig. 9, second row, third column). At altitudes above ∼ 40 km, i.e., at altitudes even somewhat lower than for ERA-Interim, there is a strong anti-correlation between zonal wind and gravity wave drag, likely related to the model sponge layer (see Fig. 9, second row, right column). Therefore, similarly as for ERA-Interim, patterns of gravity wave drag are probably not very realistic at altitudes above ∼ 40 km.

8.3 MERRA-2

For MERRA-2, in the whole altitude range 30–70 km, we find generally very strong positive correlation between gravity wave drag and du/dz (see Fig. 9, third row, third column). Similarly to JRA-55, for altitudes below ∼ 45 km the MERRA-2 correlations do not show much interannual variation, which is different for ERA-Interim and SABER gravity wave drag, and may indicate differences in details of the driving of the QBO.

For the altitude range 45–70 km, the positive correlations are qualitatively in agreement with the SABER correlations. As was shown in Sect. 5.2.2 and 5.2.3, the nonorographic gravity wave drag scheme in MERRA-2 was tuned in a way to minimize the assimilation increment due to MLS obser-

vations. Therefore, MERRA-2 even simulates a reasonable SAO in the years before 2004 when no MLS data are available and the model is relatively unconstrained in the middle mesosphere. The qualitative agreement with the SABER correlations seems to indicate that the physical mechanisms of the SAO driving by gravity waves are – at least to some extent – realistically simulated by the MERRA-2 nonorographic gravity wave drag scheme.

Note that above ~ 65 km the correlation between gravity wave drag and $\mathrm{d}u/\mathrm{d}z$ is even more positive for the years after 2004 that are fully covered by MLS observations, likely reflecting the positive influence of assimilating MLS data in MERRA-2. At altitudes above ~ 65 km, there is a strong anti-correlation between gravity wave drag and zonal wind, which is likely caused by the sponge layer near the model top (see Fig. 9, third row, right column).

8.4 ERA-5

In the altitude range below ~ 45 km ERA-5 shows interannual variability of the positive correlation between gravity wave drag and $\mathrm{d}u/\mathrm{d}z$ that is similar to the ERA-Interim and SABER correlations. However, in the altitude range 45–65 km there is no clear positive correlation between gravity wave drag and $\mathrm{d}u/\mathrm{d}z$ as would be expected from SABER observations. This indicates that the gravity wave driving of the SSAO and the SAO in the middle mesosphere is not realistic and might be linked to the model imbalances that lead to the unrealistically strong eastward jets around 60 km altitude (see Fig. 9, fourth row, third column).

The strong positive correlation in the altitude range 65–70 km seems to be related to the gravity wave drag at the top of the eastward jets that leads to the wind reversals toward westward winds and the formation of the MSAO in ERA-5. In this altitude range positive correlations are also found for SABER (see Fig. 8). However, strongest values of SABER MFz-proxy-|GWD| are found at somewhat higher altitudes and are correlated with absolute wind speed rather than with $\mathrm{d}u/\mathrm{d}z$. This correlation is not found in ERA-5 (see Fig. 9, fourth row, right column). On the one hand, this means that the model sponge in ERA-5 is not as pronounced as in the other reanalyses. On the other hand, however, the different characteristics of ERA-5 gravity wave drag and SABER observations might indicate that in ERA-5 high gravity wave phase speeds are underrepresented in the MSAO region, i.e., not all physical mechanisms that lead to the formation of the MSAO are correctly represented in ERA-5. In addition, the unrealistic SAO at lower altitudes can lead to an unrealistic wind filtering of the gravity wave spectrum, which can also affect the simulation of the MSAO.

9 Summary and discussion

In this study, we have investigated the driving of the semi-annual oscillation (SAO) of the zonal wind in the tropics by gravity waves. The study covers the whole middle atmosphere from 30–90 km altitude and focuses on the latitude band 10° S–10° N and the 2002–2018 time period of available satellite data.

First, the SAO was investigated in four different reanalyses, the ERA-Interim and ERA-5 reanalyses of the European Centre for Medium-Range Weather Forecasts (ECMWF), the JRA-55 reanalysis of the Japan Meteorological Agency (JMA), and the MERRA-2 reanalysis of the National Aeronautics and Space Administration (NASA). The expected drag due to small-scale gravity waves was estimated as the sum of the residual (*missing drag*) in the transformed Eulerian mean (TEM) zonal momentum budget and of the drag due to resolved waves of zonal wavenumbers larger than 20. All reanalyses are capable of simulating a SAO in the stratopause region (SSAO) and showing the expected asymmetry of gravity wave drag with enhanced eastward gravity wave drag during eastward wind shear. Westward-directed gravity wave drag is usually much weaker. This asymmetry is expected, because the zonal wind of the quasi-biennial oscillation (QBO) in the stratosphere has a stronger westward phase such that a larger part of the gravity wave spectrum at westward-directed phase speeds encounters critical levels in the stratosphere and cannot propagate into the stratopause region and the mesosphere (see Dunkerton, 1982; Hamilton and Mahlmann, 1988; Ern et al., 2015).

MERRA-2 and ERA-5 cover a larger altitude range than ERA-Interim and JRA-55. MERRA-2 applies stronger damping only above ~ 58 km, uses a nonorographic gravity wave parameterization, and assimilates Microwave Limb Sounder (MLS) data in the stratosphere and mesosphere. Therefore MERRA-2 produces a reasonable SAO also in the middle mesosphere, and the SAO in the stratopause region is likely more realistic than in ERA-Interim and JRA-55. On average, also in the middle mesosphere the eastward gravity wave driving of the SAO in MERRA-2 is stronger than the westward driving. However, there is strong interannual variability, and there are several episodes of strong westward-directed gravity wave driving, e.g., in the year 2006. This strong interannual variability is also supported by satellite observations of the SAO gravity wave driving (Ern et al., 2015).

Similarly to MERRA-2, ERA-5 also uses a nonorographic gravity wave parameterization, but ERA-5 does not assimilate MLS data. While the SSAO still looks realistic, the SAO eastward jets at altitudes around 60 km are overly strong, a fact that has already been reported in previous studies (Hersbach et al., 2018; Shepherd et al., 2018) and which was improved in the operational ECMWF model after 11 July 2017 (Hersbach et al., 2018). Among the four reanalyses investigated here, ERA-5 is the only reanalysis that simulates the

mesopause SAO (MSAO) above 70 km with a strong wind reversal above the middle mesosphere SAO eastward jets.

We have also investigated the SAO based on satellite observations. According to the findings of Smith et al. (2017), quasi-geostrophic winds derived from satellite observations and interpolated into the tropics give reasonable results at altitudes below about 75–80 km. Based on quasi-geostrophic zonal winds derived from MLS observations, averaged over ascending and descending parts of the satellite orbit, we found that the SAO in the lower and middle mesosphere agrees remarkably well with the SAO in MERRA-2. Only in the upper mesosphere and in the mesopause region MLS zonal winds seem to have an eastward bias compared to the other data sets. Possibly, this bias is caused by tidal effects that do not completely cancel out by averaging over ascending and descending orbit data. (Data of ascending and descending MLS orbit parts are observed at different local solar time (LST), about 13:45 LST for ascending and 01:45 LST for descending data.)

To investigate the gravity wave driving of the SAO based on satellite data, we have derived absolute gravity wave momentum fluxes and a proxy for absolute gravity wave drag (SABER MFz-proxy-|GWD|) from SABER temperature observations. SABER observations are not at fixed local solar times, because the TIMED satellite is in a slowly precessing orbit. To capture the local-solar-time-dependent effect of tides, as well as to account for the reduced reliability of interpolated quasi-geostrophic winds at altitudes above ~ 75 km, a combined data set of ERA-Interim, interpolated SABER quasi-geostrophic winds, and winds directly observed by TIDI has been composed that should represent realistic background conditions for those gravity waves that are observed by the SABER instrument.

We found that SABER MFz-proxy-|GWD| has two maxima: one maximum in the stratopause region seems to be related to the SSAO, and the other maximum in the upper mesosphere seems to be related to the MSAO. Further, in a large altitude range from the stratopause region, where the SSAO has its amplitude maximum, to about 75 km, SABER MFz-proxy-|GWD| is mainly enhanced during eastward vertical wind shear du/dz. This modulation confirms that in the stratopause region and in the middle mesosphere gravity waves mainly contribute to the driving of the eastward phase of the SAO and its downward propagation with time. This asymmetry is caused by the asymmetric wave filtering by the QBO in the stratosphere. Further, because low-phase-speed gravity waves encounter critical levels already due to the QBO in the stratosphere, it is expected that in addition to critical level filtering also saturation of gravity waves apart from critical levels will play an important role in the stratopause region and the middle mesosphere.

In the altitude range 75–80 km where the MSAO has its amplitude maximum, there is a structural change in the gravity wave interaction with the background wind. Maxima of SABER MFz-proxy-|GWD| are no longer observed in re-gions of strong du/dz but in regions where the absolute zonal wind maximizes. Simultaneously, the downward propagation rate of the SAO eastward and westward wind phases is much reduced. This finding supports the theoretical expectation that gravity waves of high phase speed, that are relatively insensitive to changes in the background wind, generally saturate. Since the spectrum is dominated by gravity waves that propagate opposite to the zonal wind in the stratopause region and middle mesosphere, this results in wave drag that is opposite to the wind direction at lower altitudes and leads to the well-known out-of-phase relationship or even anti-correlation of the MSAO zonal wind and the SAO zonal wind at lower altitudes.

These findings were confirmed by a correlation analysis investigating the temporal correlation between SABER MFz-proxy-|GWD| and different zonal wind data sets, separately for each year, for an average over the whole period 2002–2018, and for the complete 2002–2018 time series as a whole. It is found that the results are robust for the combined data set of SABER and TIDI winds, regardless of whether ascending and descending orbit data are averaged or whether ascending-only or descending-only data are considered. The same is true if just SABER interpolated quasi-geostrophic winds are used or whether winds of the SPARC climatology are used as atmospheric background. Only for the case of MLS interpolated quasi-geostrophic winds is the correlation between SABER MFz-proxy-|GWD| and MLS absolute zonal winds in the altitude range 75–80 km widely absent, attributable to an eastward bias of MLS winds in the upper MLT.

At altitudes above about 85 km we do not find strong correlations between SABER MFz-proxy-|GWD| and the SAO zonal winds. Instead, SABER MFz-proxy-|GWD| seems to be phase-locked with the tidal wind component of the SABER interpolated quasi-geostrophic winds, which becomes most obvious if ascending and descending data are treated separately. This clearly indicates that gravity waves interact with the tides. However, an in-depth investigation of this effect is difficult and beyond the scope of our study.

Analysis of the correlation between background wind and gravity wave drag derived from the reanalyses reveals that positive correlation between gravity wave drag and du/dz is indeed found for ERA-Interim, JRA-55, and MERRA-2. ERA-Interim and JRA-55, however, are strongly limited by the sponge layers close to their model tops. Particularly, MERRA-2 seems to benefit from the assimilation of MLS data and from tuning of the gravity wave drag parameterization, such that positive correlations between gravity wave drag and du/dz are seen in a large altitude range in the mesosphere, in agreement with SABER observations. However, MERRA-2 does not simulate a proper MSAO, because it is limited by the model sponge layer above 70 km. ERA-5 does not seem to have such a strong model sponge and simulates the MSAO. However, enhanced gravity wave drag is not correlated with the magnitude of MSAO winds, which might

indicate that not all parts of the gravity wave spectrum are realistically simulated by the nonorographic gravity wave parameterization.

Magnitudes of SABER MFz-proxy-|GWD| peak values are about $1–2\,\mathrm{m\,s^{-1}\,d^{-1}}$ in the stratopause region and about $20–30\,\mathrm{m\,s^{-1}\,d^{-1}}$ in the altitude range around $80\,\mathrm{km}$. It is expected that the total gravity wave driving should be stronger than indicated by the SABER MFz-proxy-|GWD|, because SABER observes only a certain part of the gravity wave spectrum (in particular, only horizontal wavelengths longer than about $100–200\,\mathrm{km}$). Further, the SABER observations are affected by observational filter effects that should result in a low bias of SABER MFz-proxy-|GWD| (see, for example, Trinh et al., 2015; Ern et al., 2018). Still, it might be possible that SABER MFz-proxy-|GWD| could be an overestimation, because no directional information is available, and there could be contributions of eastward and westward drag that do not cancel. However, such effects would make it difficult to explain the close relationship between positive $\mathrm{d}u/\mathrm{d}z$ and the SABER MFz-proxy-|GWD| in the stratopause region and middle mesosphere. Further, the SABER observations in the stratopause region are roughly in agreement with lidar observations (e.g., Deepa et al., 2006; Antonita et al., 2007) that also cover only a certain part of the whole spectrum of gravity waves.

Although values of SABER MFz-proxy-|GWD| are likely strongly biased low, they are roughly in agreement with simulations of the SAO by free-running general circulation models (e.g., Richter and Garcia, 2006; Osprey et al., 2010; Peña-Ortiz et al., 2010). This indicates that gravity wave drag in free-running models is likely too weak. This is further supported by the fact that the gravity wave drag in free-running models is much lower than our estimates from the four reanalyses considered here, and also lower than estimates by Lieberman et al. (2010) based on TIMED observations in the mesopause region. Indeed, in a recent model intercomparison Smith et al. (2020) concluded that in free-running general circulation models too weak gravity wave forcing would be one of the main reasons for misrepresentations of the SSAO. Still, because our gravity wave observations do not provide any directional information, the magnitudes of net gravity wave momentum flux and of net gravity wave drag remain an open issue that needs to be addressed by better global observations providing information about the full 3D structure of gravity waves (see also, for example, Preusse et al., 2014; Ern et al., 2017; Gumbel et al., 2020).

References

Alexander, M. J.: Global and seasonal variations in three-dimensional gravity wave momentum flux from satellite limb-sounding temperatures, Geophys. Res. Lett., 42, 6860–6867, https://doi.org/10.1002/2015GL065234, 2015.

Alexander, M. J. and Rosenlof, K. H.: Nonstationary gravity wave forcing of the stratospheric zonal mean wind, J. Geophys. Res., 101, 23465–23474, 1996.

Alexander, M. J., Geller, M., McLandress, C., Polavarapu, S., Preusse, P., Sassi, F., Sato, K., Eckermann, S. D., Ern, M., Hertzog, A., Kawatani, Y., Pulido, M., Shaw, T., Sigmond, M., Vincent, R., and Watanabe, S.: Recent developments in gravity-wave effects in climate models and the global distribution of gravity-wave momentum flux from observations and models, Q. J. Roy. Meteor. Soc., 136, 1103–1124, https://doi.org/10.1002/qj.637, 2010.

Andrews, D. G., Holton, J. R., and Leovy, C. B.: Middle atmosphere dynamics, Academic Press, Orlando, Fl., 489 pp., 1987.

Anstey, J. A. and Shepherd, T. G.: High-latitude influence of the quasi-biennial oscillation, Q. J. Roy. Meteor. Soc., 140, 1–21, 2014.

Antonita, T. M., Ramkumar, G., Kishore Kumar, K., Appu, K. S., and Namboothiri, K. V. S.: A quantitative study on the role of gravity waves in driving the tropical Stratospheric Semiannual Oscillation, J. Geophys. Res., 112, D12115, https://doi.org/10.1029/2006JD008250, 2007.

Baldwin, M. P., Gray, L. J., Dunkerton, T. J., Hamilton, K., Haynes, P. H., Randel, W. J., Holton, J. R., Alexander, M. J., Hirota, I., Horinouchi, T., Jones, D. B. A., Kinnersley, J. S., Marquardt, C., Sato, K., and Takahashi, M.: The quasi-biennial oscillation, Rev. Geophys., 39, 179–229, 2001.

Baron, P., Murtagh, D. P., Urban, J., Sagawa, H., Ochiai, S., Kasai, Y., Kikuchi, K., Khosrawi, F., Körnich, H., Mizobuchi, S., Sagi, K., and Yasui, M.: Observation of horizontal winds in the middle-atmosphere between 30° S and 55° N during the northern winter 2009–2010, Atmos. Chem. Phys., 13, 6049–6064, https://doi.org/10.5194/acp-13-6049-2013, 2013.

Becker, E. and Vadas, S. L.: Secondary gravity waves in the winter mesosphere: Results from a high-resolution global circulation model, J. Geophys. Res.-Atmos., 123, 2605–2627, https://doi.org/10.1002/2017JD027460, 2018.

Beres, J. H., Garcia, R. R., Boville, B. A., and Sassi, F.: Implementation of a gravity wave source spectrum parameterization dependent on the properties of convection in the Whole Atmosphere Community Climate Model (WACCM), J. Geophys. Res., 110, D10108, https://doi.org/10.1029/2004JD005504, 2005.

Burrage, M. D., Vincent, R. A., Mayr, H. G., Skinner, W. R., Arnold, N. F., and Hays, P. B.: Long-term variability in the equatorial middle atmosphere zonal wind, J. Geophys. Res., 101, 12847–12854, 1996.

Chen, D., Strube, C., Ern, M., Preusse, P., and Riese, M.: Global analysis for periodic variations in gravity wave squared amplitudes and momentum fluxes in the middle atmosphere, Ann. Geophys., 37, 487–506, https://doi.org/10.5194/angeo-37-487-2019, 2019.

Day, K. A. and Mitchell, N. J.: Mean winds in the MLT, the SQBO and MSAO over Ascension Island (8° S, 14° W), Atmos. Chem. Phys., 13, 9515–9523, https://doi.org/10.5194/acp-13-9515-2013, 2013.

Dee, D. P., Uppala, S. M., Simmons, A. J., Berrisford, P., Poli, P., Kobayashi, S., Andrae, U., Balmaseda, M. A., Balsamo, G., Bauer, P., Bechtold, P., Beljaars, A. C. M., van de Berg, L., Bidlot, J., Bormann, N., Delsol, C., Dragani, R., Fuentes, M., Geer, A. J., Haimberger, L., Healy, S. B., Hersbach, H., Holm, E. V., Isaksen, L., Kallberg, P., Koehler, M., Matricardi, M., McNally, A. P., Monge-Sanz, B. M., Morcrette, J.-J., Park, B.-K., Peubey, C., de Rosnay, P., Tavolato, C., Thepaut, J.-N., and Vitart, F.: The ERA-Interim reanalysis: configuration and performance of the data assimilation system, Q. J. Roy. Meteor. Soc., 137, 553–597, https://doi.org/10.1002/qj.828, 2011 (data available at: https://apps.ecmwf.int/archive-catalogue/?class=ei, last access: 7 September 2021).

Deepa, V., Ramkumar, G., and Krishna Murthy, B. V.: Gravity waves observed from the Equatorial Wave Studies (EWS) campaign during 1999 and 2000 and their role in the generation of

stratospheric semiannual oscillations, Ann. Geophys., 24, 2481–2491, https://doi.org/10.5194/angeo-24-2481-2006, 2006.

Delisi, D. P. and Dunkerton, T. J.: Equatorial semiannual oscillation in zonally averaged temperature observed by the Nimbus 7 SAMS and LIMS, J. Geophys. Res., 93, 3899–3904, 1988a.

Delisi, D. P. and Dunkerton, T. J.: Seasonal variation of the semiannual oscillation, J. Atmos. Sci., 45, 2772–2787, 1988b.

Dhadly, M. S., Emmert, J. T., Drob, D. P., McCormack, J. P., and Niciejewski, R.: Short-term and interannual variations of migrating diurnal and semidiurnal tides in the mesosphere and lower thermosphere, J. Geophys. Res.-Space, 123, 7106–7123, https://doi.org/10.1029/2018JA025748, 2018.

Dunkerton, T. J.: Theory of the mesopause semiannual oscillation, J. Atmos. Sci., 39, 2681–2690, 1982.

Dunkerton, T. J.: The role of gravity waves in the quasi-biennial oscillation, J. Geophys. Res., 102, 26053–26076, 1997.

Dunkerton, T. J. and Delisi, D. P.: Interaction of the quasi-biennial oscillation and the stratopause semiannual oscillation, J. Geophys. Res., 102, 26107–26116, 1997.

Ebdon, R. A.: The quasi-biennial oscillation and its association with tropospheric circulation patterns, Meteorol. Mag., 104, 282–297, 1975.

England, S. L., Dobbin, A., Harris, M. J., Arnold, N. F., and Aylward, A. D.: A study into the effects of gravity wave activity on the diurnal tide and airglow emissions in the equatorial mesosphere and lower thermosphere using the Coupled Middle Atmosphere and Thermosphere (CMAT) general circulation model, J. Atmos. Sol.-Terr. Phy., 68, 293–308, https://doi.org/10.1016/j.jastp.2005.05.006, 2006.

Ern, M., Preusse, P., Alexander, M. J., and Warner, C. D.: Absolute values of gravity wave momentum flux derived from satellite data, J. Geophys. Res., 109, D20103, https://doi.org/10.1029/2004JD004752, 2004.

Ern, M., Preusse, P., Krebsbach, M., Mlynczak, M. G., and Russell III, J. M.: Equatorial wave analysis from SABER and ECMWF temperatures, Atmos. Chem. Phys., 8, 845–869, https://doi.org/10.5194/acp-8-845-2008, 2008.

Ern, M., Lehmann, C., Kaufmann, M., and Riese, M.: Spectral wave analysis at the mesopause from SCIAMACHY airglow data compared to SABER temperature spectra, Ann. Geophys., 27, 407–416, https://doi.org/10.5194/angeo-27-407-2009, 2009.

Ern, M., Preusse, P., Gille, J. C., Hepplewhite, C. L., Mlynczak, M. G., Russell III, J. M., and Riese, M.: Implications for atmospheric dynamics derived from global observations of gravity wave momentum flux in stratosphere and mesosphere, J. Geophys. Res., 116, D19107, https://doi.org/10.1029/2011JD015821, 2011.

Ern, M., Preusse, P., Kalisch, S., Kaufmann, M., and Riese, M.: Role of gravity waves in the forcing of quasi two-day waves in the mesosphere: An observational study, J. Geophys. Res.-Atmos., 118, 3467–3485, https://doi.org/10.1029/2012JD018208, 2013.

Ern, M., Ploeger, F., Preusse, P., Gille, J. C., Gray, L. J., Kalisch, S., Mlynczak, M. G., Russell III, J. M., and Riese, M.: Interaction of gravity waves with the QBO: A satellite perspective, J. Geophys. Res.-Atmos., 119, 2329–2355, https://doi.org/10.1002/2013JD020731, 2014.

Ern, M., Preusse, P., and Riese, M.: Driving of the SAO by gravity waves as observed from satellite, Ann. Geophys., 33, 483–504, https://doi.org/10.5194/angeo-33-483-2015, 2015.

Ern, M., Trinh, Q. T., Kaufmann, M., Krisch, I., Preusse, P., Ungermann, J., Zhu, Y., Gille, J. C., Mlynczak, M. G., Russell III, J. M., Schwartz, M. J., and Riese, M.: Satellite observations of middle atmosphere gravity wave absolute momentum flux and of its vertical gradient during recent stratospheric warmings, Atmos. Chem. Phys., 16, 9983–10019, https://doi.org/10.5194/acp-16-9983-2016, 2016.

Ern, M., Hoffmann, L., and Preusse, P.: Directional gravity wave momentum fluxes in the stratosphere derived from high-resolution AIRS temperature data, Geophys. Res. Lett., 44, 475–485, https://doi.org/10.1002/2016GL072007, 2017.

Ern, M., Trinh, Q. T., Preusse, P., Gille, J. C., Mlynczak, M. G., Russell III, J. M., and Riese, M.: GRACILE: a comprehensive climatology of atmospheric gravity wave parameters based on satellite limb soundings, Earth Syst. Sci. Data, 10, 857–892, https://doi.org/10.5194/essd-10-857-2018, 2018.

Fujiwara, M., Wright, J. S., Manney, G. L., Gray, L. J., Anstey, J., Birner, T., Davis, S., Gerber, E. P., Harvey, V. L., Hegglin, M. I., Homeyer, C. R., Knox, J. A., Krüger, K., Lambert, A., Long, C. S., Martineau, P., Molod, A., Monge-Sanz, B. M., Santee, M. L., Tegtmeier, S., Chabrillat, S., Tan, D. G. H., Jackson, D. R., Polavarapu, S., Compo, G. P., Dragani, R., Ebisuzaki, W., Harada, Y., Kobayashi, C., McCarty, W., Onogi, K., Pawson, S., Simmons, A., Wargan, K., Whitaker, J. S., and Zou, C.-Z.: Introduction to the SPARC Reanalysis Intercomparison Project (S-RIP) and overview of the reanalysis systems, Atmos. Chem. Phys., 17, 1417–1452, https://doi.org/10.5194/acp-17-1417-2017, 2017.

Fritts, D. C.: Gravity wave saturation in the middle atmosphere: A review of theory and observations, Rev. Geophys., 22, 275–308, 1984.

Fritts, D. C. and Alexander, M. J.: Gravity wave dynamics and effects in the middle atmosphere, Rev. Geophys., 41, 1003, https://doi.org/10.1029/2001RG000106, 2003.

Fritts, D. C. and Vincent, R. A.: Mesospheric momentum flux studies at Adelaide, Australia: observations and a gravity wave–tidal interaction model, J. Atmos. Sci., 44, 605–619, 1987.

Fritts, D. C., Garten, J. F., Riggin, D. M., Goldberg, R. A., Lehmacher, G. A., Schmidlin, F. J., McCarthy, S., Kudeki, E., Fawcett, C. D., Hitchman, M. H., Lieberman, R. S., Reid, I. M., and Vincent, R. A.: Equatorial dynamics observed by rocket, radar, and satellite during the CADRE/MALTED campaign, 2. Mean and wave structures, coherence, and variability, J. Geophys. Res., 102, 26191–26216, 1997.

Garcia, R. R. and Boville, B. A.: Downward control of the mean meridional circulation and temperature distribution of the polar winter stratosphere, J. Atmos. Sci., 51, 2238–2245, 1994.

Garcia, R. R. and Clancy, R. T.: Seasonal variation in equatorial mesospheric temperature observed by SME, J. Atmos. Sci., 47, 1666–1673, 1990.

Garcia, R. R. and Sassi, F.: Modulation of the mesospheric semiannual oscillation by the quasibiennial oscillation, Earth Planets Space, 51, 563–569, 1999.

Garcia, R. R., Dunkerton, T. J., Lieberman, R. S., and Vincent, R. A.: Climatology of the semiannual oscillation of the tropical middle atmosphere, J. Geophys. Res., 102, 26,019–26,032, 1997.

Garcia, R. R., Lieberman, R., Russell III, J. M., and Mlynczak, M. G.: Large-scale waves in the mesosphere

and lower thermosphere observed by SABER, J. Atmos. Sci., 62, 4384–4399, 2005.

GATS Inc.: SABER Level 2A data (version 2), GATS Inc. [data set], Newport News, VA, USA, available at: http://saber.gats-inc.com/browse_data.php, last access: 7 September 2021.

Gelaro, R., McCarty, W., Suarez, M. J., Todling, R., Molod, A., Takacs, L., Randles, C., Darmenov, A., Bosilovich, M. G., Reichle, R., Wargan, K., Coy, L., Cullather, R., Draper, C., Akella, S., Buchard, V., Conaty, A., da Silva, A., Gu, W., Kim, G.-K., Koster, R., Lucchesi, R., Merkova, D., Nielsen, J. E., Partyka, G., Pawson, S., Putman, W., Rienecker, M., Schubert, S. D., Sienkiewicz, M., and Zhao, B.: The Modern-Era Retrospective Analysis for Research and Applications, Version 2 (MERRA-2), J. Climate, 30, 5419–5454, https://doi.org/10.1175/JCLI-D-16-0758.1, 2017.

Geller, M. A., Alexander, M. J., Love, P. T., Bacmeister, J., Ern, M., Hertzog, A., Manzini, E., Preusse, P., Sato, K., Scaife, A. A., and Zhou, T.: A comparison between gravity wave momentum fluxes in observations and climate models, J. Climate, 26, 6383–6405, https://doi.org/10.1175/JCLI-D-12-00545.1, 2013.

Global Modeling and Assimilation Office (GMAO): MERRA-2 inst3_3d_asm_Nv: 3d, 3-Hourly, Instantaneous, Model-Level, Assimilation, Assimilated Meteorological Fields V5.12.4, Goddard Earth Sciences Data and Information Services Center (GES DISC) [data set], Greenbelt, MD, USA, https://doi.org/10.5067/WWQSXQ8IVFW8, 2015a.

Global Modeling and Assimilation Office (GMAO): MERRA-2 tavg3_3d_udt_Np: 3d, 3-Hourly, Time-Averaged, Pressure-Level, Assimilation, Wind Tendencies V5.12.4, Goddard Earth Sciences Data and Information Services Center (GES DISC) [data set], Greenbelt, MD, USA, https://doi.org/10.5067/CWV0G3PPPWFW, 2015b.

Gray, L. J., Brown, M. J., Knight, J., Andrews, M., Lu, H., O'Reilly, C., and Anstey, J.: Forecasting extreme stratospheric polar vortex events, Nat. Commun., 11, 4630, https://doi.org/10.1038/s41467-020-18299-7, 2020.

Groves, G. V.: Annual and semiannual zonal wind components and corresponding temperature and density variations, 60–130 km, Planet. Space Sci., 20, 2099–2112, 1972.

Gumbel, J., Megner, L., Christensen, O. M., Ivchenko, N., Murtagh, D. P., Chang, S., Dillner, J., Ekebrand, T., Giono, G., Hammar, A., Hedin, J., Karlsson, B., Krus, M., Li, A., McCallion, S., Olentšenko, G., Pak, S., Park, W., Rouse, J., Stegman, J., and Witt, G.: The MATS satellite mission – gravity wave studies by Mesospheric Airglow/Aerosol Tomography and Spectroscopy, Atmos. Chem. Phys., 20, 431–455, https://doi.org/10.5194/acp-20-431-2020, 2020.

Gurubaran, S. and Rajaram, R.: Mean winds, tides, and gravity waves during the westward phase of the mesopause semiannual oscillation (MSAO), J. Geophys. Res., 106, 31817–31824, 2001.

Hamilton, K.: Rocketsonde observations of the mesospheric semiannual oscillation at Kwajalein, Atmos. Ocean, 20, 281–286, 1982.

Hamilton, K. and Mahlmann, J. D.: General Circulation Model simulation of the semiannual oscillation of the tropical middle atmosphere, J. Atmos. Sci., 45, 3212–3235, 1988.

Hays, P. B., Arbreu, V. J., Dobbs, M. E., Gell, D. A., Grassl, H. J., and Skinner, W. R.: The high-resolution Doppler imager on the Upper Atmosphere Research Satellite, J. Geophys. Res., 98, 10713–10723, 1993.

Hersbach, H. and Dee, D.: ERA5 reanalysis is in production, ECMWF Newsletter, Vol. 147, 7, available at: https://www.ecmwf.int/en/newsletter/147/news/era5-reanalysis-production (last access: 1 March 2021), 2016.

Hersbach, H., de Rosnay, P., Bell, B., Schepers, D., Simmons, A., Soci, C., Abdalla, S., Alonso Balmaseda, M., Balsamo, G., Bechtold, P., Berrisford, P., Bidlot, J., de Boisséson, E., Bonavita, M., Browne, P., Buizza, R., Dahlgren, P., Dee, D., Dragani, R., Diamantakis, M., Flemming, J., Forbes, R., Geer, A., Haiden, T., Hólm, E., Haimberger, L., Hogan, R., Horányi, A., Janisková, M., Laloyaux, P., Lopez, P., Muñoz-Sabater, J., Peubey, C., Radu, R., Richardson, D., Thépaut, J.-N., Vitart, F., Yang, X., Zsótér, E., and Zuo, H.: Operational global reanalysis: progress, future directions and synergies with NWP, ERA Report Series, 27, 1–63, https://doi.org/10.21957/tkic6g3wm, 2018 (data available at: https://apps.ecmwf.int/data-catalogues/era5/?class=ea, last access: 7 September 2021).

Hersbach, H., Bell, B., Paul, B., András, H., Sabater, J. M., Nicolas, J., Radu, R., Schepers, D., Simmons, A., Soci, C., and Dee, D.: Global reanalysis: goodbye ERA-Interim, hello ERA-5, ECMWF Newsletter, No. 159, 17–24, https://doi.org/10.21957/vf291hehd7, 2019.

Hersbach, H., Bell, B., Berrisford, P., Hirahara, S., Horányi, A., Munoz-Sabater, J., Nicolas, J., Peubey, C., Radu, R., Schepers, D., Simmons, A., Soci, C., Abdalla, S., Abellan, X., Balsamo, G., Bechtold, P., Biavati, G., Bidlot, J., Bonavita, M., de Chiara, G., Dahlgren, P., Dee, D., Diamantakis, M., Dragani, R., Flemming, J., Forbes, R., Fuentes, M., Geer, A., Haimberger, L., Healy, S., Hogan, R. J., Hólm, E., Janisková, M., Keeley, S., Laloyaux, P., Lopez, P., Lupu, C., Radnoti, G., de Rosnay, P., Rozum, I., Vamborg, F., Villaume, S., and Thépaut, J.-N.: The ERA5 Global Reanalysis, Q. J. Roy. Meteor. Soc., 146, 1999–2049, https://doi.org/10.1002/qj.3803, 2020.

Hirota, I.: Equatorial waves in the upper stratosphere and mesosphere in relation to the semiannual oscillation of the zonal wind, J. Atmos. Sci., 35, 714–722, 1978.

Hirota, I.: Observational evidence of the semiannual oscillation in the tropical middle atmosphere – A review, Pure Appl. Geophys., 118, 217–238, 1980.

Holton, J. R.: The generation of mesospheric planetary waves by zonally asymmetric gravity wave breaking, J. Atmos. Sci., 41, 3427–3430, 1984.

Holton, J. R. and Tan, H.-C.: The influence of the equatorial quasi-biennial oscillation on the global circulation at 50 mb, J. Atmos. Sci., 37, 2200–2208, 1980.

Huang, F. T., Mayr, H. G., Reber, C. A., Russell III, J. M., Mlynczak, M. G., and Mengel, J. G.: Ozone quasi-biennial oscillations (QBO), semiannual oscillations (SAO), and correlations with temperature in the mesosphere, lower thermosphere, and stratosphere, based on measurements from SABER on TIMED and MLS on UARS, J. Geophys. Res., 113, A01316, https://doi.org/10.1029/2007JA012634, 2008.

Iwasaki, T., Yamada, S., and Tada, K.: A parameterization scheme of orographic gravity wave drag with the different vertical partitionings, Part I: Impact on medium range forecasts, J. Meteorol. Soc. Jpn., 67, 11–27, 1989a.

Iwasaki, T., Yamada, S., and Tada, K.: A parameterization scheme of orographic gravity wave drag with the different vertical partitionings, Part II: Zonally averaged budget analyses based on transformed Eulerian-mean method, J. Meteorol. Soc. Jpn., 67, 29–41, 1989b.

Japan Meteorological Agency (JMA): JRA-55: Japanese 55-year Reanalysis, Daily 3-Hourly and 6-Hourly Data, updated monthly, Research Data Archive at the National Center for Atmospheric Research, Computational and Information Systems Laboratory [data set], https://doi.org/10.5065/D6HH6H41, 2013.

Jewtoukoff, V., Hertzog, A., Plougonven, R., de la Camara, A., and Lott, F.: Comparison of gravity waves in the southern hemisphere derived from balloon observations and the ECMWF analyses, J. Atmos. Sci., 72, 3449–3468, https://doi.org/10.1175/JAS-D-14-0324.1, 2015.

Kang, M.-J., Chun, H.-Y., Kim, Y.-H., Preusse, P., and Ern, M.: Momentum flux of convective gravity waves derived from an offline gravity wave parameterization. Part II: Impacts on the Quasi-Biennial Oscillation, J. Atmos. Sci., 75, 3753–3775, https://doi.org/10.1175/JAS-D-18-0094.1, 2018.

Kawatani, Y., Hirooka, T., Hamilton, K., Smith, A. K., and Fujiwara, M.: Representation of the equatorial stratopause semiannual oscillation in global atmospheric reanalyses, Atmos. Chem. Phys., 20, 9115–9133, https://doi.org/10.5194/acp-20-9115-2020, 2020.

Kidston, J., Scaife, A. A., Hardiman, S. C., Mitchell, D. M., Butchart, N., Baldwin, M. P., and Gray, L. J.: Stratospheric influence on tropospheric jet streams, storm tracks and surface weather, Nat. Geosci., 8, 433–440, https://doi.org/10.1038/NGEO2424, 2015.

Killeen, T. L., Wu, Q., Solomon, S. C., Ortland, D. A., Skinner, W. R., Niciejewski, R. J., and Gell, D. A.: TIMED Doppler Interferometer: Overview and recent results, J. Geophys. Res., 111, A10S01, https://doi.org/10.1029/2005JA011484, 2006.

Kim, Y.-H., Bushell, A. C., Jackson, D. R., and Chun, H.-Y.: Impacts of introducing a convective gravity-wave parameterization upon the QBO in the Met Office Unified Model, Geophys. Res. Lett., 40, 1873–1877, https://doi.org/10.1002/grl.50353, 2013.

Kim, Y.-J., Eckermann, S. D., and Chun, H.-Y.: An overview of the past, present and future of gravity-wave drag parameterization for numerical climate and weather prediction models – Survey article, Atmos. Ocean, 41, 65–98, https://doi.org/10.3137/ao.410105, 2003.

Kishore Kumar, G., Kishore Kumar, K., Singer, W., Zülicke, C., Gurubaran, S., Baumgarten, G., Ramkumar, G., Sathishkumar, S., and Rapp, M.: Mesosphere and lower thermosphere zonal wind variations over low latitudes: Relation to local stratospheric zonal winds and global circulation anomalies, J. Geophys. Res.-Atmos., 119, 5913–5927, https://doi.org/10.1002/2014JD021610, 2014.

Kobayashi, S., Ota, Y., Harada, Y., Ebita, A., Moriya, M., Onoda, H., Onogi, K., Kamahori, H., Kobayashi, C., Endo, H., Miyaoka, K., and Takahashi, K.: The JRA-55 Reanalysis: General Specifications and Basic Characteristics, J. Meteorol. Soc. Jpn., 93, 5–48, https://doi.org/10.2151/jmsj.2015-001, 2015.

Kovalam, S., Vincent, R. A., and Love, P.: Gravity waves in the equatorial MLT region, J. Atmos. Sol.-Terr. Phy., 68, 266–282, https://doi.org/10.1016/j.jastp.2005.05.009, 2006.

Krebsbach, M., and Preusse, P.: Spectral analysis of gravity wave activity in SABER temperature data, Geophys. Res. Lett., 34, L03814, https://doi.org/10.1029/2006GL028040, 2007.

Krismer, T. R., Giorgetta, M. A., and Esch, M.: Seasonal aspects of the quasi-biennial oscillation in the Max Planck Institute Earth System Model and ERA-40, J. Adv. Model. Earth Sy., 5, 406–421, https://doi.org/10.1002/jame.20024, 2013.

Kuai, L., Shia, R.-L., Jiang, X., Tung, K.-K., and Yung, Y. L.: Nonstationary synchronization of equatorial QBO with SAO in observations and a model, J. Atmos. Sci., 66, 1654–1664, 2009.

Kumar, K. K., Swain, D., John, S. R., and Ramkumar, G.: Simultaneous observations of SAO and QBO in winds, temperature and ozone in the tropical middle atmosphere over Thumba (8.5N, 77E), Clim. Dynam., 37, 1961–1973, 2011.

Lieberman, R. S., Burrage, M. D., Gell, D. A., Hays, P. B., Marshall, A. R., Ortland, D. A., Skinner, W. R., Wu, D. L., Vincent, R. A., and Franke, S. J.: Zonal mean winds in the equatorial mesosphere and lower thermosphere observed by the High Resolution Doppler Imager, Geophys. Res. Lett., 20, 2849–2852, 1993.

Lieberman, R. S., Riggin, D. M., Garcia, R. R., Wu, Q., and Remsberg, E. E.: Observations of intermediate-scale diurnal waves in the equatorial mesosphere and lower thermosphere, J. Geophys. Res., 111, A10S11, https://doi.org/10.1029/2005JA011498, 2006.

Lieberman, R. S., Ortland, D. A., Riggin, D. M., Wu, Q., and Jacobi, C.: Momentum budget of the migrating diurnal tide in the mesosphere and lower thermosphere, J. Geophys. Res., 115, D20105, https://doi.org/10.1029/2009JD013684, 2010.

Lindzen, R. S.: Turbulence and stress owing to gravity wave and tidal breakdown, J. Geophys. Res., 86, 9707–9714, 1981.

Lindzen, R. S.: On the development of the theory of the QBO, B. Am. Meteorol. Soc., 68, 329–337, 1987.

Lindzen, R. S. and Holton, J. R.: A theory of the quasi-biennial oscillation, J. Atmos. Sci., 25, 1095–1107, 1968.

Liu, X., Xu, J., Yue, J., Liu, H. L., and Yuan, W.: Large winds and wind shears caused by the nonlinear interactions between gravity waves and tidal backgrounds in the mesosphere and lower thermosphere, J. Geophys. Res.-Space, 119, 7698–7708, https://doi.org/10.1002/2014JA020221, 2014.

Livesey, N. J., Read, W. G., Wagner, P. A., Froidevaux, L., Lambert, A., Manney, G. L., Millan Valle, L. F., Pumphrey, H. C., Santee, M. L., Schwartz, M. J., Wang, S., Fuller, R. A., Jarnot, R. F., Knosp, B. W., Martinez, E., and Ray, R.: Earth Observing System (EOS) Aura Microwave Limb Sounder (MLS) Version 4.2x Level 2 data quality and description document, Version 4.2x-3.1, Tech. Rep. JPL D-33509 Rev. D, Jet Propulsion Lab., California Institute of Technology, Pasadena, California 91109-8099, 1–169, 2017.

Lott, F. and Miller, M. J.: A new subgrid-scale orographic drag parametrization: Its formulation and testing, Q. J. Roy. Meteor. Soc., 123, 101–127, 1997.

Marshall, A. G. and Scaife, A. A.: Impact of the QBO on surface winter climate, J. Geophys. Res., 114, D18110, https://doi.org/10.1029/2009JD011737, 2009.

Martineau, P., Wright, J. S., Zhu, N., and Fujiwara, M.: Zonal-mean data set of global atmospheric reanalyses on pressure levels, Earth Syst. Sci. Data, 10, 1925–1941, https://doi.org/10.5194/essd-10-1925-2018, 2018.

Matsumoto, N., Shinbori, A., Riggin, D. M., and Tsuda, T.: Measurement of momentum flux using two meteor radars in Indonesia, Ann. Geophys., 34, 369–377, https://doi.org/10.5194/angeo-34-369-2016, 2016.

Matthias, V. and Ern, M.: On the origin of the mesospheric quasi-stationary planetary waves in the unusual Arctic winter 2015/2016, Atmos. Chem. Phys., 18, 4803–4815, https://doi.org/10.5194/acp-18-4803-2018, 2018.

Mayr, H. G., Mengel, J. G., Chan, K. L., and Porter, H. S.: Mesosphere dynamics with gravity wave forcing: Part I. Diurnal and semi-diurnal tides, J. Atmos. Sol.-Terr. Phy., 63, 1851–1864, 2001.

McFarlane, N. A.: The effect of orographically excited gravity-wave drag on the circulation of the lower stratosphere and troposphere, J. Atmos. Sci., 44, 1775–1800, 1987.

McLandress, C.: The Seasonal Variation of the Propagating Diurnal Tide in the Mesosphere and Lower Thermosphere. Part I: The Role of Gravity Waves and Planetary Waves, J. Atmos. Sci., 59, 893–906, 2002.

Mengel, J. G., Mayr, H. G., Chan, K. L., Hines, C. O., Reddy, C. A., Arnold, N. F., and Porter, H. S.: Equatorial oscillations in the middle atmosphere generated by small scale gravity waves, Geophys. Res. Lett., 22, 3027–3030, 1995.

Mlynczak, M. G.: Energetics of the mesosphere and lower thermosphere and the SABER instrument, Adv. Space Res., 44, 1177–1183, 1997.

Molod, A., Takacs, L., Suarez, M., and Bacmeister, J.: Development of the GEOS-5 atmospheric general circulation model: evolution from MERRA to MERRA2, Geosci. Model Dev., 8, 1339–1356, https://doi.org/10.5194/gmd-8-1339-2015, 2015.

NASA GES DISC: The MLS Level 2 geopotential height product (version 4.2), NASA Goddard Earth Sciences Data and Information Services Center [data set], available at: https://acdisc.gesdisc.eosdis.nasa.gov/data/Aura_MLS_Level2/ML2GPH.004/, last access: 7 September 2021a.

NASA GES DISC: The MLS Level 2 temperature product (version 4.2), NASA Goddard Earth Sciences Data and Information Services Center [data set], available at: https://acdisc.gesdisc.eosdis.nasa.gov/data/Aura_MLS_Level2/ML2T.004/, last access: 7 September 2021b.

NCAR HAO: The TIDI vector wind product (version 03.07a), NCAR High Altitude Observatory [data set], available at: http://download.hao.ucar.edu/archive/tidi/data/vec0307a/, last access: 7 September 2021.

Niciejewski, R., Wu, Q., Skinner, W., Gell, D., Cooper, M., Marshall, A., Killeen, T., Solomon, S., and Ortland, D.: TIMED Doppler Interferometer on the Thermosphere Ionosphere Mesosphere Energetics and Dynamics satellite: Data product overview, J. Geophys. Res., 111, A11S90, https://doi.org/10.1029/2005JA011513, 2006.

Oberheide, J., Lehmacher, G. A., Offermann, D., Grossmann, K. U., Manson, A. H., Meek, C. E., Schmidlin, F. J., Singer, W., Hoffmann, P., and Vincent, R. A.: Geostrophic wind fields in the stratosphere and mesosphere from satellite data, J. Geophys. Res., 107, 8175, https://doi.org/10.1029/2001JD000655, 2002.

Oberheide, J., Wu, Q., Killeen, T. L., Hagan, M. E., and Roble, R. G.: Diurnal nonmigrating tides from TIMED Doppler Interferometer wind data: Monthly climatologies and seasonal variations, J. Geophys. Res., 111, A10S03, https://doi.org/10.1029/2005JA011491, 2006.

Orr, A., Bechtold, P., Scinocca, J. F., Ern, M., and Janiskova, M.: Improved middle atmosphere climate and forecasts in the ECMWF model through a nonorographic gravity wave drag parameterization, J. Climate, 23, 5905–5926, https://doi.org/10.1175/2010JCLI3490.1, 2010.

Ortland, D. A. and Alexander, M. J.: Gravity wave influence on the global structure of the diurnal tide in the mesosphere and lower thermosphere, J. Geophys. Res., 111, A10S10, https://doi.org/10.1029/2005JA011467, 2006.

Osprey, S. M., Gray, L. J., Hardiman, S. C., Butchart, N., Bushell, A. C., and Hinton, T. J.: The climatology of the middle atmosphere in a vertically extended version of the Met Office's climate model. Part II: Variability, J. Atmos. Sci., 67, 3637–3651, https://doi.org/10.1175/2010JAS3338.1, 2010.

Palo, S. E. and Avery, S. K.: Mean winds and the semiannual oscillation in the mesosphere and lower thermosphere at Christmas Island, J. Geophys. Res., 98, 20385–20400, 1993.

Pascoe, C. L., Gray, L. J., and Scaife, A. A.: A GCM study of the influence of equatorial winds on the timing of sudden stratospheric warmings, Geophys. Res. Lett., 33, L06825, https://doi.org/10.1029/2005GL024715, 2006.

Peña-Ortiz, C., Schmidt, H., Giorgetta, M. A., and Keller, M.: QBO modulation of the semiannual oscillation in MAECHAM5 and HAMMONIA, J. Geophys. Res., 115, 8178, https://doi.org/10.1029/2001JD000699, 2010.

Polichtchouk, I., Hogan, R. J., Shepherd, T. G., Bechtold, P., Stockdale, T., Malardel, S., Lock, S.-J., and Magnusson, L.: What influences the middle atmosphere circulation in the IFS?, ECMWF Technical Memorandum, 809, 1–48, 2017.

Preusse, P., Eckermann, S. D., Oberheide, J., Hagan, M. E., and Offermann, D.: Modulation of gravity waves by tides as seen in CRISTA temperatures, Adv. Space Res., 27, 1773–1778, 2001.

Preusse, P., Dörnbrack, A., Eckermann, S. D., Riese, M., Schaeler, B., Bacmeister, J. T., Broutman, D., and Grossmann, K. U.: Space-based measurements of stratospheric mountain waves by CRISTA, 1. Sensitivity, analysis method, and a case study, J. Geophys. Res., 106, 8178, https://doi.org/10.1029/2001JD000699, 2002.

Preusse, P., Schroeder, S., Hoffmann, L., Ern, M., Friedl-Vallon, F., Ungermann, J., Oelhaf, H., Fischer, H., and Riese, M.: New perspectives on gravity wave remote sensing by spaceborne infrared limb imaging, Atmos. Meas. Tech., 2, 299–311, https://doi.org/10.5194/amt-2-299-2009, 2009.

Preusse, P., Ern, M., Bechtold, P., Eckermann, S. D., Kalisch, S., Trinh, Q. T., and Riese, M.: Characteristics of gravity waves resolved by ECMWF, Atmos. Chem. Phys., 14, 10483–10508, https://doi.org/10.5194/acp-14-10483-2014, 2014.

Randel, W., Chanin, M.-L., Michaut, C., and the SPARC Reference Climatology Group: SPARC intercomparison of middle atmosphere climatologies, WCRP 116, WMO/TD No. 1142, SPARC report No. 3, 2002.

Randel, W., Udelhofen, P., Fleming, E., Geller, M., Gelman, M., Hamilton, K., Karoly, D., Ortland, D., Pawson, S., Swinbank, R., Wu, F., Baldwin, M., Chanin, M.-L., Keckhut, P., Labitzke, K., Remsberg, E., Simmons, A., and Wu, D. L.: The SPARC intercomparison of middle-atmosphere climatologies, J. Climate, 17, 986–1003, 2004.

Rapp, M., Dornbrack, A., and Preusse, P.: Large midlatitude stratospheric temperature variability caused by inertial instability: A potential source of bias for gravity wave climatologies, Geophys. Res. Lett., 45, 10682–10690, https://doi.org/10.1029/2018GL079142, 2018.

Reed, R. J.: Some features of the annual temperature regime in the tropical stratosphere, Mon. Weather Rev., 90, 211–215, 1962.

Reed, R. J.: Zonal wind behavior in the equatorial stratosphere and lower mesosphere, J. Geophys. Res., 71, 4223–4233, 1966.

Remsberg, E. E., Gordley, L. L., Marshall, B. T., Thompson, R. E., Burton, J., Bhatt, P., Harvey, V. L., Lingenfelser, G., and Natarajan, M.: The Nimbus 7 LIMS version 6 radiance conditioning and temperature retrieval methods and results, J. Quant. Spectrosc. Ra., 86, 395–424, https://doi.org/10.1016/j.jqsrt.2003.12.007, 2004.

Remsberg, E. E., Marshall, B. T., Garcia-Comas, M., Krueger, D., Lingenfelser, G. S., Martin-Torres, J., Mlynczak, M. G., Russell III, J. M., Smith, A. K., Zhao, Y., Brown, C., Gordley, L. L., Lopez-Gonzalez, M. J., Lopez-Puertas, M., She, C.-Y., Taylor, M. J., and Thompson, R. E.: Assessment of the quality of the Version 1.07 temperature-versus-pressure profiles of the middle atmosphere from TIMED/SABER, J. Geophys. Res., 113, D17101, https://doi.org/10.1029/2008JD010013, 2008.

Ribstein, B. and Achatz, U.: The interaction between gravity waves and solar tides in a linear tidal model with a 4-D ray-tracing gravity-wave parameterization, J. Geophys. Res.-Space, 121, 8936–8950, https://doi.org/10.1002/2016JA022478, 2016.

Richter, J. H. and Garcia, R. R.: On the forcing of the mesospheric semi-annual oscillation in the Whole Atmosphere Community Climate Model, Geophys. Res. Lett., 33, L01806, https://doi.org/10.1029/2005GL024378, 2006.

Russell III, J. M., Mlynczak, M. G., Gordley, L. L., Tansock, J., and Esplin, R.: An overview of the SABER experiment and preliminary calibration results, Proc. SPIE, 3756, 277–288, 1999.

Sandu, I., Beljaars, A., Bechtold, P., Mauritsen, T., and Balsamo, G.: Why is it so difficult to represent stably stratified conditions in numerical weather prediction (NWP) models?, J. Adv. Model. Earth Sy., 5, 117–133, https://doi.org/10.1002/jame.20013, 2013.

Sassi, F. and Garcia, R. R.: The role of equatorial waves forced by convection in the tropical semi-annual oscillation, J. Atmos. Sci., 54, 1925–1942, 1997.

Sato, K., Yasui, R., and Miyoshi, Y.: The momentum budget in the stratosphere, mesosphere, and lower thermosphere. Part I: contributions of different wave types and in situ generation of Rossby waves, J. Atmos. Sci., 75, 3613–3633, https://doi.org/10.1175/JAS-D-17-0336.1, 2018.

Scaife, A. A., Athanassiadou, M., Andrews, M., Arribas, A., Bald- win, M., Dunstone, N., Knight, J., MacLachlan, C., Manzini, E., Müller, W. A., Pohlmann, H., Smith, D., Stockdale, T., and Williams, A.: Predictability of the quasi-biennial oscillation and its northern winter teleconnection on seasonal to decadal timescales, Geophys. Res. Lett., 41, 1752–1758, https://doi.org/10.1002/2013GL059160, 2014.

Schroeder, S., Preusse, P., Ern, M., and Riese, M.: Gravity waves resolved in ECMWF and measured by SABER, Geophys. Res. Lett., 36, L10805, https://doi.org/10.1029/2008GL037054, 2009.

Schwartz, M. J., Lambert, A., Manney, G. L., Read, W. G., Livesey, N. J., Froidevaux, L., Ao, C. O., Bernath, P. F., Boone, C. D., Cofield, R. E., Daffer, W. H., Drouin, B. J., Fet-

zer, E. J., Fuller, R. A., Jarnot, R. F., Jiang, J. H., Jiang, Y. B., Knosp, B. W., Krüger, K., Li, J.-L. F., Mlynczak, M. G., Pawson, S., Russell III, J. M., Santee, M. L., Snyder, W. V., Stek, P. C., Thurstans, R. P., Tompkins, A. M., Wagner, P. A., Walker, K. A., Waters, J. W., and Wu, D. L.: Validation of the Aura Microwave Limb Sounder temperature and geopotential height measurements, J. Geophys. Res., 113, D15S11, https://doi.org/10.1029/2007JD008783, 2008.

Shepherd, T. G., Polichtchouk, I., Hogan, R. J., and Simmons, A. J.: Report on Stratosphere Task Force, ECMWF Technical Memorandum, 824, 1–32, https://doi.org/10.21957/0vkp0t1xx, 2018.

Shu, J., Tian, W., Hu, D., Zhang, J., Shang, L., Tian, H., and Xie, F.: Effects of the Quasi-Biennial Oscillation and Stratospheric Semiannual Oscillation on tracer transport in the upper stratosphere, J. Atmos. Sci., 70, 1370–1389, https://doi.org/10.1175/JAS-D-12-053.1, 2013.

Simmons, A., Soci, C., Nicolas, J., Bell, B., Berrisford, P., Dragani, R., Flemming, J., Haimberger, L., Healy, S., Hersbach, H., Horányi, A., Inness, A., Munoz-Sabater, J., Radu, R., and Schepers, D.: Global stratospheric temperature bias and other stratospheric aspects of ERA5 and ERA5.1, ECMWF Technical Memorandum, 859, 1–38, https://doi.org/10.21957/rcxqfmg0, 2020.

Smith, A. K.: The origin of stationary planetary waves in the upper mesosphere, J. Atmos. Sci., 60, 3033–3041, 2003.

Smith, A. K.: Global dynamics of the MLT, Surv. Geophys., 33, 1177–1230, https://doi.org/10.1007/s10712-012-9196-9, 2012.

Smith, A. K., Garcia, R. R., Moss, A. C., and Mitchell, N. J.: The semiannual oscillation of the tropical zonal wind in the middle atmosphere derived from satellite geopotential height retrievals, J. Atmos. Sci., 74, 2413–2425, https://doi.org/10.1175/JAS-D-17-0067.1, 2017.

Smith, A. K., Holt, L. A., Garcia, R. R., Anstey, J. A., Serva, F., Butchart, N., Osprey, S., Bushell, A. C., Kawatani, Y., Kim, Y.-H., Lott, F., Braesicke, P., Cagnazzo, C., Chen, C.-C., Chun, H.-Y., Gray, L., Kerzenmacher, T., Naoe, H., Richter, J., Versick, S., Schenzinger, V., Watanabe, S., and Yoshida, K.: The equatorial stratospheric semiannual oscillation and time-mean winds in QBOi models, Q. J. Roy. Meteor. Soc., 1–17, https://doi.org/10.1002/qj.3690, 2020.

Song, R., Kaufmann, M., Ern, M., Ungermann, J., Liu, G., and Riese, M.: Three-dimensional tomographic reconstruction of atmospheric gravity waves in the mesosphere and lower thermosphere (MLT), Atmos. Meas. Tech., 11, 3161–3175, https://doi.org/10.5194/amt-11-3161-2018, 2018.

SPARC: Temperature and Zonal Wind Climatology, SPARC Data Centre [data set], available at: ftp://sparc-ftp1.ceda.ac.uk/sparc/ref_clim/randel/temp_wind/ (last access: 7 September 2021), 2002.

Sridharan, S.: Seasonal variations of low-latitude migrating and nonmigrating diurnal and semidiurnal tides in TIMED-SABER temperature and their relationship with source variations, J. Geophys. Res.-Space, 124, 3558–3572, https://doi.org/10.1029/2018JA026190, 2019.

Sridharan, S. and Sathishkumar, S.: Seasonal and interannual variations of gravity wave activity in the low-latitude mesosphere and lower thermosphere over Tirunelveli (8.7° N, 77.8° E), Ann. Geophys., 26, 3215–3223, https://doi.org/10.5194/angeo-26-3215-2008, 2008.

Strube, C., Ern, M., Preusse, P., and Riese, M.: Removing spurious inertial instability signals from gravity wave temperature perturbations using spectral filtering methods, Atmos. Meas. Tech., 13, 4927–4945, https://doi.org/10.5194/amt-13-4927-2020, 2020.

Swinbank, R. and Ortland, D. A.: Compilation of wind data for the UARS Reference Atmosphere Project, J. Geophys. Res., 108, 4615, https://doi.org/10.1029/2002JD003135, 2003.

Tang, Y., Dou, X., Li, T., Nakamura, T., Xue, X., Huang, C., Manson, A., Meek, C., Thorsen, D., and Avery, S.: Gravity wave characteristics in the mesopause region revealed from OH airglow imager observations over Northern Colorado, J. Geophys. Res.-Space, 119, 630–645, https://doi.org/10.1002/2013JA018955, 2014.

Trinh, Q. T., Kalisch, S., Preusse, P., Chun, H.-Y., Eckermann, S. D., Ern, M., and Riese, M.: A comprehensive observational filter for satellite infrared limb sounding of gravity waves, Atmos. Meas. Tech., 8, 1491–1517, https://doi.org/10.5194/amt-8-1491-2015, 2015.

Venkateswara Rao, N., Tsuda, T., and Kawatani, Y.: A remarkable correlation between short period gravity waves and semiannual oscillation of the zonal wind in the equatorial mesopause region, Ann. Geophys., 30, 703–710, https://doi.org/10.5194/angeo-30-703-2012, 2012.

Vincent, R. A.: The dynamics of the mesosphere and lower thermosphere: a brief review, Progress in Earth and Planetary Science, 2, 4, https://doi.org/10.1186/s40645-015-0035-8, 2015.

Warner, C. D., Scaife, A. A., and Butchart, N.: Filtering of parameterized nonorographic gravity waves in the Met Office unified model, J. Atmos. Sci., 62, 1831–1848, 2005.

Watanabe, S., Kawatani, Y., Tomikawa, Y., Miyazaki, K., Takahashi, M., and Sato, K.: General aspects of a T213L256 middle atmosphere general circulation model, J. Geophys. Res., 113, D12110, https://doi.org/10.1029/2008JD010026, 2008.

Waters, J. W., Froidevaux, L., Harwood, R. S., Jarnot, R. F., Pickett, H. M., Read, W. G., Siegel, P. H., Cofield, R. E., Filipiak, M. J., Flower, D. A., Holden, J. R., Lau, G. K., Livesey, N. J., Manney, G. L., Pumphrey, H. C., Santee, M. L., Wu, D. L., Cuddy, D. T., Lay, R. R., Loo, M. S., Perun, V. S., Schwartz, M. J., Stek, P. C., Thurstans, R. P., Boyles, M. A., Chandra, K. M., Chavez, M. C., Chen, G.-S., Chudasama, B. V., Dodge, R., Fuller, R. A., Girard, M. A., Jiang, J. H., Jiang, Y., Knosp, B. W., LaBelle, R. C., Lam, J. C., Lee, K. A., Miller, D., Oswald, J. E., Patel, N. C., Pukala, D. M., Quintero, O., Scaff, D. M., Van Snyder, W., Tope, M. C., Wagner, P. A., and Walch, M. J.: The Earth Observing System Microwave Limb Sounder (EOS MLS) on the Aura Satellite, IEEE T. Geosci. Remote, 44, 1075–1092, https://doi.org/10.1109/TGRS.2006.873771, 2006.

Wu, Q., Ortland, D. A., Solomon, S. C., Skinner, W. R., and Niciejewski, R. J.: Global distribution, seasonal, and interannual variations of mesospheric semidiurnal tide observed by TIMED TIDI, J. Atmos. Sol.-Terr. Phy., 73, 2482–2502, https://doi.org/10.1016/j.jastp.2011.08.007, 2011.

Zhu, Y., Kaufmann, M., Ern, M., and Riese, M.: Nighttime atomic oxygen in the mesopause region retrieved from SCIA-MACHY O(^{1}S) green line measurements and its response to solar cycle variation, J. Geophys. Res.-Space, 120, 9057–9073, https://doi.org/10.1002/2015JA021405, 2015.